Int J Fract (2025) 249:30
https://doi.org/10.1007/s10704-025-00848-0

RESEARCH

Approximate analytical solutions for the energy release rate of planar cracks in constrained elastic thin layers

Sida Hao · Rui Huang · Gregory J. Rodin

Received: 18 October 2024 / Accepted: 5 March 2025 / Published online: 18 March 2025

Abstract Within the context of linear elasticity, approximate analytical solutions are developed for the energy release rate for axisymmetric planar cracks in elastic thin layers sandwiched between two rigid plates. These solutions are validated by comparing them with finite element solutions, and they are applicable to cracks in constrained thin layers made of compressible, nearly incompressible, or incompressible materials. These analytical solutions provide insights into the effects of geometry and material compressibility on fracture of thin layers. In particular, stability of crack growth is discussed under both displacement and force-controlled loading conditions, summarized in stability maps. Remarkably, it is found that, under force-controlled conditions, stable crack growth is possible in incompressible or nearly incompressible layers, but not in compressible layers. We compare the energy release rates for embedded and interfacial cracks, showing that they differ when the cracks are small but become approximately equal for large cracks. The analytical approach is further extended to non-axisymmetric planar cracks in compressible thin layers. However, a similar extension does not apply for cracks in incompressible or nearly incompressible layers.

S. Hao · R. Huang · G.J. Rodin (✉)
Department of Aerospace Engineering and Engineering Mechanics, University of Texas, Austin, TX 78712, USA
e-mail: gjr@oden.utexas.edu

G.J. Rodin
Oden Institute for Computational Engineering and Sciences, University of Texas, Austin, TX 78712, USA

Keywords Thin layer · Energy release rate · Axisymmetric crack · Interfacial crack · Stability

1 Introduction

Soft thin layers constrained by stiff materials are commonly used in engineering applications, such as bearings, sealants, and adhesives (Kelly and Konstantinidis 2011; Warn and Ryan 2012; Shull and Creton 2004; Biggins et al. 2013; Creton and Ciccotti 2016; Lin et al. 2017). This paper is concerned with fracture of constrained thin layers under tension. In particular, we restrict our attention to internal, as opposed to edge, cracks in sandwich structures in which a soft thin layer is constrained between two stiff plates. It has been established experimentally that fracture of such layers can be either cohesive or adhesive. Cohesive fracture occurs as a result of nucleation and growth of cracks embedded in the layers, as observed in many experiments (Gent and Lindley 1959; Lindsey 1967; Fond 2001; Bayraktar et al. 2008; Kumar and Lopez-Pamies 2021; Guo and Ravi-Chandar 2023). In contrast, adhesive fracture occurs as a result of nucleation and growth of cracks along the interfaces, also observed in many experiments (Lin et al. 2000; Webber et al. 2003; Minsky and Turner 2015; Fischer et al. 2017; Hensel et al. 2019).

This paper focuses on approximate analytical approaches to determining the energy release rate G for both embedded and interfacial cracks, since G is

central to quantifying conditions for initiation and stability of crack growth. Our approach is based on formal asymptotic analysis of uncracked elastic thin layers by Movchan et al. (2021, 2023). Although this approach is limited to the linear elastic setting, it allows one to seamlessly analyze layers made of compressible, nearly incompressible, or incompressible materials, and for cracks of both small and large sizes. The accuracy of the approximate analytical solutions is assessed by comparing them to convergent finite element solutions. To our knowledge, only a subset of such solutions for G have appeared previously, such as those for axisymmetric embedded cracks in compressible layers, small embedded cracks in incompressible layers, and small interfacial cracks (Crosby et al. 2000; Benvidi and Bacca 2021). Although in all cases G can be calculated numerically, the approximate analytical solutions provide additional insights into the effects of geometry and material compressibility on fracture of elastic thin layers. Remarkably, the approximate analytical solutions can be extended to non-axisymmetric planar cracks in compressible thin layers, although a similar extension does not apply for cracks in incompressible or nearly incompressible layers.

Our analysis also deals with stability of crack growth, especially possible arrest of crack growth in thin layers formed by nearly incompressible or incompressible materials. In the context of linear elasticity, this effect has been discussed by Benvidi and Bacca (2021) and Horváth and Kossa (2024), based on finite element calculations of G for axisymmetric interfacial cracks including both internal and edge cracks. For thin layers of nearly incompressible materials, Benvidi and Bacca (2021) found that the internal center cracks are more likely to grow than the edge cracks. In this work, we focus on internal cracks. Furthermore, Hao et al. (2023) demonstrated that arrest of crack growth is also possible for axisymmetric cracks embedded in thin layers formed by incompressible neo-Hookean materials.

The remainder of the paper is structured as follows. In Sect. 2, we present two sets of approximate analytical solutions for G for axisymmetric embedded cracks. The first set is for small cracks, whose size is much smaller than the layer thickness, and the second set is for large cracks, whose size is much larger than the layer thickness. In Sect. 3, these two sets of solutions are exploited to analyze stability of crack growth under either displacement- or force-controlled boundary conditions. In Sect. 4, the approximate analytical solutions developed for embedded cracks are extended to axisymmetric interfacial cracks. In Sect. 5, we compare the energy release rates for the axisymmetric embedded and interfacial cracks. In Sect. 6, approximate analytical solutions are developed for non-axisymmetric planar cracks in thin layers formed by compressible materials. In Sect. 7, we conclude the paper with a summary of the results. For completeness, the asymptotic solutions for uncracked layers used for the development of the approximate analytical solutions for cracked layers are presented in the appendix.

2 Axisymmetric problems for embedded cracks

2.1 Problem statement

Consider a circular solid cylindrical layer whose thickness is $2h$ and radius is a (Fig. 1). This layer is described in cylindrical coordinates, such that

$$-h \le z \le h \quad \text{and} \quad r \le a\,. \tag{1}$$

The layer is perfectly bonded to two rigid plates at the bases $z = \pm h$. The layer contains an embedded circular crack of radius c. The crack is confined to the plane $z = 0$, and its center coincides with that of the layer.

We are interested in determining the energy release rate G along the crack front, as a result of pulling the plates apart along the z-axis, so that the upper plate is displaced by Δ and the lower plate is displaced by $-\Delta$. We analyze this problem in the context of the classical theory of linear elasticity, by assigning to the layer material a shear modulus μ and Poisson's ratio ν. We assume that the layer is thin, so that $h \ll a$.

For the configuration in Fig. 1, we construct two approximate analytical solutions for G. The first solution is for small cracks characterized by the inequality $c \ll h$. The second solution is for large cracks, characterized by two inequalities, $c \gg h$ and $a - c \gg h$. Thus, *both* the radius of the crack c and the uncracked ligament $a - c$ are large compared to the thickness of the layer. We regard the two approximate analytical solutions as general because they are valid for any Poisson's ratio, including $\nu = 1/2$ for incompressible materials. This generality is particularly important for problems involving layers formed by nearly incompressible materials.

The problems of interest involve three dimensionless parameters. The first one is the normalized thickness,

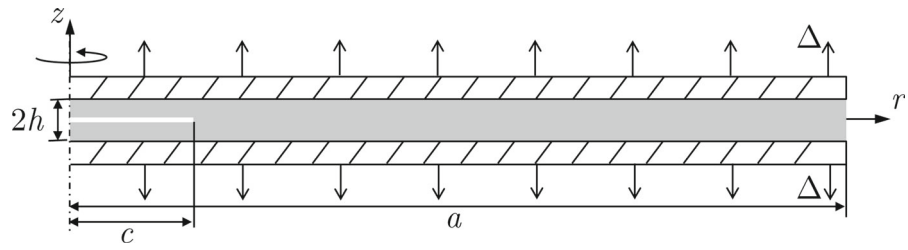

Fig. 1 An embedded circular crack of radius c lying in the mid-plane of a thin layer of radius a and thickness $2h$, constrained between two rigid plates and loaded symmetrically by a displacement Δ

$$\xi := \frac{h}{a} \ll 1 \,. \tag{2}$$

The second parameter represents material compressibility,

$$\chi := \sqrt{\frac{3(1-2\nu)}{2(1-\nu)}} \,. \tag{3}$$

This parameter was first introduced by Lindsey et al. (1963), and it arises naturally in formal asymptotic analysis of uncracked elastic thin layers (Movchan et al. 2021, 2023). It is clear that $\chi = 0$ represents incompressible materials. For nearly incompressible materials, $\chi \ll 1$; for compressible materials, with ν significantly different from $1/2$, $\chi = \mathcal{O}(1)$. The parameter χ is essential for characterization of thin layers formed by nearly incompressible materials. In this regard, let us recall the classical results of Stefan (1874), Reynolds (1886), and Filon (1902) for the apparent Young modulus, which takes into account that the layer is constrained. For an incompressible material (Stefan 1874; Reynolds 1886)

$$\tilde{E} = \frac{3\mu}{8\xi^2} \,, \tag{4}$$

whereas for a compressible underlying material (Filon 1902),

$$\bar{E} = \frac{3\mu}{\chi^2} \,. \tag{5}$$

The use of these two equations becomes problematic for thin layers formed by nearly incompressible materials, simply because it is unclear which one to choose. This issue has been addressed in Movchan et al. (2021) who introduced the ratio

$$\zeta := \frac{\xi}{\chi} \,. \tag{6}$$

Then, for layers characterized by $\zeta \gg 1$, the material incompressibility prevails, and Eq. (4) is the right choice. In contrast, for layers characterized by $\zeta \ll 1$, the layer thinness prevails, and Eq. (5) is the right choice. However, for layers characterized by $\zeta = \mathcal{O}(1)$, a different and more complicated expression has to be used (Movchan et al. 2021). We regard such layers as nearly incompressible. Thus, while a nearly incompressible material is characterized by the condition $\chi \ll 1$, a nearly incompressible layer is characterized by the condition $\zeta = \mathcal{O}(1)$. Note that a nearly incompressible thin layer is necessarily formed by a nearly incompressible material because the conditions $\zeta = \mathcal{O}(1)$ and $\xi \ll 1$ imply $\chi = \mathcal{O}(\xi) \ll 1$. But a nearly incompressible material may form a compressible layer if $\xi \ll \chi$. For example, for a rubber layer characterized by $\nu = 0.499905$ (Anderson et al. 2004) and $\xi = 0.001$, the parameter $\zeta \approx 0.04$, and therefore its apparent Young modulus is better represented by Eq. (5) than Eq. (4).

The third dimensionless parameter is the normalized crack size:

$$\varsigma := \frac{c}{a} \,. \tag{7}$$

This choice of normalizing the crack radius is not natural for small cracks, for which a better parameter is c/h. Of course, the two normalizations are related as

$$\frac{c}{h} = \frac{\varsigma}{\xi} \,. \tag{8}$$

Since the theory of linear elasticity dictates that the energy release rate G is a quadratic function of Δ, it is useful to normalize G as

$$G = g\,(\xi, \chi, \varsigma) \times \mu h \left(\frac{\Delta}{h}\right)^2 \,. \tag{9}$$

Here g is a dimensionless function of the three dimensionless parameters. The chosen dimensional group is meaningful, but certainly not unique. Throughout the paper, variants of g are used to present both analytical and numerical solutions. We distinguish among those variants by using subscripts, superscripts, and listing their arguments.

In this work, the accuracy of the approximate analytical solutions is assessed by comparing them with convergent finite element solutions, which are straightforward to obtain using the standard features of ABAQUS,

Table 1 The values of Poisson's ratio ν and the material compressibility parameter χ for the benchmark materials

Material Type	CM	NIM1	NIM2	IM
ν	0.3	0.49	0.4999	0.5
χ	0.9258	0.2425	0.0245	0

including axisymmetric hybrid elements (CAX8H and CAX6H), quarter-point elements at the tip of the crack, and the J-integral to calculate the energy release rate G. We use the hybrid elements uniformly in all cases, although they are not necessary for the cases with compressible materials. In those cases, the standard displacement-based elements can be used to reduce the computing time, but using hybrid elements does not cause additional errors.

The errors in the finite element solutions for G, presented in this work, were estimated to be less than 0.3%. This estimate was based on a convergence study, by comparing the solutions obtained with progressively finer meshes. Figure 2 shows the mesh used for finite element analysis of the configuration characterized by $h/a = 1/10$ and $c/h = 1$. By symmetry, only half of the layer is analyzed with the traction-free condition along the crack and the symmetry condition elsewhere along the mid-plane ($z = 0$). This mesh was generated by identifying the semicircular contours centered at the crack tip (Fig. 2b) along with uniform seeding nodes on the layer boundary. The semicircular contours around the crack tip are used for calculating the energy release rate by the J-integral method.

Throughout the paper, we consider four representative values of Poisson's ratio, $\nu = 0.3,\ 0.49,\ 0.4999,\ 0.5$. These values represent benchmark compressible (CM), nearly incompressible (NIM1 and NIM2), and incompressible (IM) materials, respectively. The values of χ corresponding to these benchmark materials are compiled in Table 1. Hereafter, we refer to layers formed by the benchmark materials simply as CM, NM1, NM2, and IM layers.

2.2 Small cracks

For small embedded cracks, $c \ll h \ll a$, and therefore a small crack can be treated as if it were embedded in an infinite body, subjected to a remote tensile stress σ_0, corresponding to the axial stress that would be transmitted through the center of the uncracked layer.

For a circular crack in an infinite body, the pertinent classical solution for the energy release rate is (Sadowsky and Sternberg 1949; Green and Sneddon 1950; Irwin 1962; Tada et al. 1973):

$$G_s^e = \frac{1-\nu}{2\mu} K_I^2 = \frac{1-\nu}{2\mu}\left(\frac{2}{\pi}\sigma_0\sqrt{\pi c}\right)^2 . \tag{10}$$

Here, the subscript s and superscript e refer to small embedded cracks, respectively, and K_I is the Mode-I stress intensity factor of the crack.

For a constrained thin layer, the stress σ_0 at the center depends on the layer thinness ξ and the material compressibility χ. A general expression for σ_0 is derived from the asymptotic solution for an uncracked layer (Movchan et al. 2021); see (A.12) in Appendix. As a result, Eq. (10) is specified as

$$G_s^e = \frac{27}{4\pi\chi^4\left(3-\chi^2\right)} \left\{2 + \frac{4\chi^6 - 24\chi^4 + 39\chi^2 - 18}{\left(3-\chi^2\right)\left[3I_0\left(\frac{\chi}{\xi}\right) - 2\xi\chi I_1\left(\frac{\chi}{\xi}\right)\right]}\right\}^2 \left(\frac{c}{h}\right) \times \mu h\left(\frac{\Delta}{h}\right)^2 , \tag{11}$$

where I_0 and I_1 are modified Bessel's functions of the first kind (Abramowitz and Stegun 1968). Then, following Eq. (9), we obtain the normalized energy release rate:

$$g_s^e\left(\xi, \chi, \frac{c}{h}\right) = \frac{27}{4\pi\chi^4\left(3-\chi^2\right)} \left\{2 + \frac{4\chi^6 - 24\chi^4 + 39\chi^2 - 18}{\left(3-\chi^2\right)\left[3I_0\left(\frac{\chi}{\xi}\right) - 2\xi\chi I_1\left(\frac{\chi}{\xi}\right)\right]}\right\}^2 \left(\frac{c}{h}\right) . \tag{12}$$

Equation (12) is valid for any $\chi > 0$. For incompressible layers characterized by $\xi/\chi \gg 1$, Eq. (12) can be simplified by taking the limit $\chi \to 0$, while fixing ξ and c/h, which yields

$$\tilde{g}_s^e\left(\xi, \frac{c}{h}\right) := \lim_{\chi\to 0} g_s^e\left(\xi, \chi, \frac{c}{h}\right) = \frac{9}{16\pi\xi^4}\left(\frac{c}{h}\right) . \tag{13}$$

For compressible layers characterized by $\xi/\chi \ll 1$, Eq. (12) can be simplified by taking the limit $\xi \to 0$, while fixing χ and c/h, which yields:

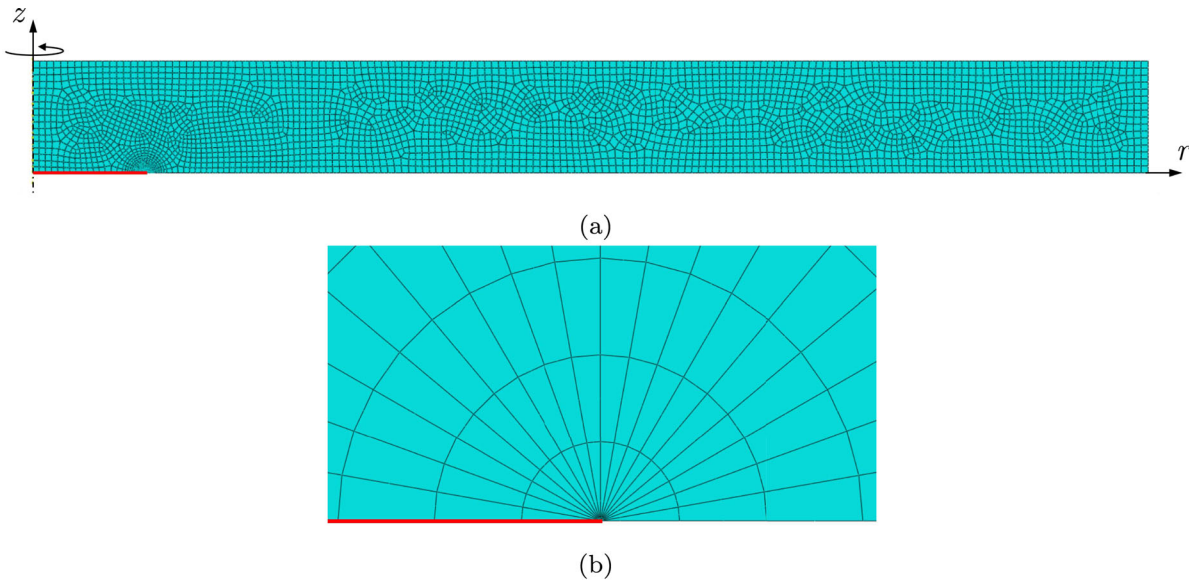

Fig. 2 **a** The mesh used for the finite element analysis of an axisymmetric embedded crack (indicated by the red line) in an elastic thin layer with $h/a = 1/10$ and $c/h = 1$. By symmetry, only the upper half of the layer is meshed. **b** The local mesh near the crack front with concentric semicircular contours. The crack face is shown in red

$$\bar{g}_s^e\left(\chi, \frac{c}{h}\right) := \lim_{\xi \to 0} g_s^e\left(\xi, \chi, \frac{c}{h}\right) = \frac{27}{\pi \chi^4 \left(3 - \chi^2\right)} \left(\frac{c}{h}\right) . \tag{14}$$

Note that g_s^e, $\tilde{g}_s^e$, and $\bar{g}_s^e$ are linear functions of c/h.

The accuracy of the functions g_s^e, $\tilde{g}_s^e$, and $\bar{g}_s^e$ is assessed in Fig. 3 by comparing them with the corresponding finite element solutions for the normalized energy release rate. In Figs. 3a,c,e, we plot the energy release rate, normalized according to Eq. (9), versus c/h for $\xi = 1/100, 1/50, 1/10$, respectively. In each of these plots, the analytical solutions, g_s^e, $\tilde{g}_s^e$, and $\bar{g}_s^e$, are shown as lines, while the finite element solutions are shown as discrete symbols. The function g_s^e in Eq. (12) is used for the NIM1 and NIM2 layers, the function $\tilde{g}_s^e$ in Eq. (13) is used for the IM layers, and the function $\bar{g}_s^e$ in Eq. (14) is used for the CM layers. In each plot, $0 < c/h < 1$, while the approximate analytical solutions are expected to be accurate only for $c/h \ll 1$. For this reason, in each plot, we show a green region defined by the inequality $c/h < 1/10$, which is adopted as a proxy for the condition $c \ll h$. The inequality $c/h < 1/10$ implies that we choose to treat $1/10$ as a small number; consequently, in what follows, 10 is treated as a large number.

In Fig. 3, we also plot the relative error,

$$e = \left| \frac{g_A - g_{FE}}{g_{FE}} \right| ,$$

versus c/h. Here, the subscripts A and FE refer to the analytical and finite element solutions, respectively. Figures 3b,d,f are paired with Figs. 3a,c,e, respectively, as each pair shares the same ξ. The plots in Figs. 3b,d indicate that the approximate analytical solutions are accurate with $e < 1\%$ for $0 < c/h < 0.1$ and $\xi = 1/100, 1/50$, although the error is slightly larger for the IM layers. For the thickest layers ($\xi = 1/10$) in Fig. 3(f), the error is much larger for the NIM1, NIM2, and IM layers. This was expected because the asymptotic expression for σ_0 is expected to be accurate only for sufficiently thin layers. Furthermore, the predictions for $e \approx 5\%$ in Fig. 3f are consistent with those in Movchan et al. (2021) for $\xi = 1/10$. Thus, the approximate analytical solutions, g_s^e, $\tilde{g}_s^e$, and $\bar{g}_s^e$ presented in Eqs. (12), (13) and (14), respectively, are accurate only for small cracks ($c/h < 0.1$) in sufficiently thin layers.

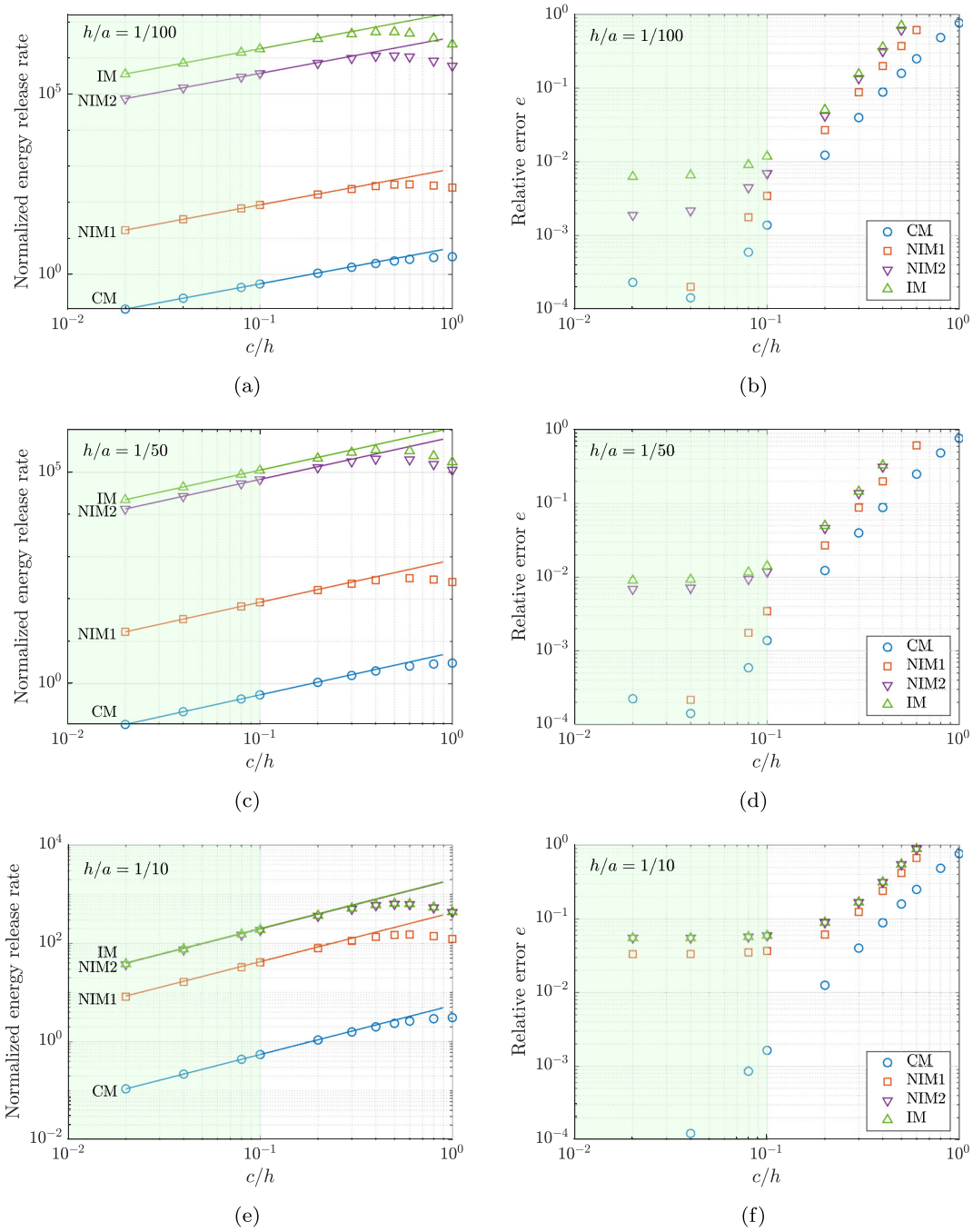

Fig. 3 The approximate analytical (lines) and finite element (symbols) solutions for small embedded cracks. **a**,**c**,**e** The energy release rate, normalized according to Eq. (9), versus c/h; **b**,**d**,**f** the relative error e of the approximate analytical solutions vis-à-vis finite element solutions versus c/h. The plots are paired so that $h/a = 1/100$ for (**a**,**b**), $h/a = 1/50$ for (**c**,**d**), and $h/a = 1/10$ for (**e**,**f**). In each plot, the approximate analytical solutions are represented by g_s^e for the NIM1 and NIM2 layers, by $\tilde{g}_s^e$ for the IM layers, and by $\bar{g}_s^e$ for the CM layers. These functions are specified in Eqs. (12), (13), and (14), respectively. The compressibility of the four materials, CM, NIM1, NIM2, and IM, are specified in Table 1. The domains of validity of the approximate analytical solutions are colored green

2.3 Large cracks

The approximate analytical solutions for large cracks ($c, a - c \gg h$) are constructed by starting with the definition of the energy release rate:

$$G = -\frac{\partial P}{\partial A_C}\,, \tag{15}$$

where P is the potential energy and A_C is the area of the crack platform. For a circular crack of radius c, the energy release rate is

$$G = -\frac{1}{2\pi c}\frac{\partial P}{\partial c}\,. \tag{16}$$

For a prescribed displacement Δ (Fig. 1), the potential energy P is equal to the strain energy in the layer and thus

$$P = F\Delta\,, \tag{17}$$

where F is the transmitted force corresponding to Δ. Therefore, we can express G as

$$G = -\frac{\Delta}{2\pi c}\frac{\partial F}{\partial c}\,. \tag{18}$$

Note that, as c increases, the layer becomes more compliant, so that F decreases, and therefore $G > 0$.

The crux of our analytical approach is that, for a large crack, the force F is calculated not for the original specimen but for an annular layer with the inner radius c and outer radius a (Fig. 4). That is, we assume that the material in the cylinders above and below the crack contributes negligibly to the force. Since $c \gg h$ and $a - c \gg h$ for large cracks, the annular layer can be treated as thin, and the force F can be calculated approximately by the asymptotic approach (see Appendix) as

$$F_l = 2\pi\int_c^a \sigma_{zz|z=h} r\,\mathrm{d}r = \frac{6\pi}{\chi^3}\left(\frac{\Delta}{h}\right)\mu a^2 \times\left\{\frac{\chi(1-\varsigma^2)}{2} + \left[I_1\left(\frac{\chi}{\xi}\right) - \varsigma I_1\left(\frac{\chi\varsigma}{\xi}\right)\right]C_1\xi - \left[K_1\left(\frac{\chi}{\xi}\right) - \varsigma K_1\left(\frac{\chi\varsigma}{\xi}\right)\right]C_2\xi\right\}\,, \tag{19}$$

with the parameters C_1 and C_2 defined in Appendix (A.16) and (A.17). In this equation, K_1 is a modified Bessel's function of the second kind (Abramowitz and Stegun 1968) and the subscript l refers to large cracks.

Although Eq. (19) is valid for any $\chi > 0$, its explicit form is too complicated to provide insight. Therefore, it is important to develop simpler expressions restricted to compressible, nearly incompressible, and incompressible layers. For IM layers ($\xi/\chi \gg 1$), this is accomplished by taking the limit as $\chi \to 0$:

$$\tilde{F}_l := \lim_{\chi\to 0} F_l = \frac{3\pi\mu a^2\left(1-\varsigma^2\right)\left[1-\varsigma^2+\left(1+\varsigma^2\right)\log\varsigma\right]\Delta}{8h\xi^2\log\varsigma}\,. \tag{20}$$

Once combined, Eqs. (9), (18), and (20) yield

$$\tilde{g}_l^e(\xi,\varsigma) = \frac{3\left(1-\varsigma^2+2\varsigma^2\log\varsigma\right)^2}{16\xi^2\varsigma^2\log^2\varsigma}\,. \tag{21}$$

For compressible layers ($\xi/\chi \ll 1$), Eq. (19) is simplified by taking the limit as $\xi \to 0$:

$$\bar{F}_l := \lim_{\xi\to 0} F_l = \frac{3\pi\mu a^2(1-\varsigma^2)\Delta}{\chi^2 h}\,. \tag{22}$$

Once combined, Eqs.(9), (18), and (22) yield

$$\bar{g}_l^e(\chi) = \frac{3}{\chi^2}\,. \tag{23}$$

For nearly incompressible layers, $\xi/\chi = \mathcal{O}(1)$, and thus neither of the above two limits is applicable. In this case, Eq. (19) is rewritten by replacing χ with ξ/ζ based on Eq. (6), so that the expression for F_l involves only one small parameter ξ. Then, by expanding the modified version of Eq. (19) into Maclaurin's series in ξ, we obtain

$$F_l = \frac{3\pi\mu a\Delta}{\xi\chi^2}\left\{1-\varsigma^2-\frac{4\xi^2}{\chi^2}\frac{1}{K_0\left(\frac{\chi}{\xi}\right)I_0\left(\frac{\chi\varsigma}{\xi}\right) - I_0\left(\frac{\chi}{\xi}\right)K_0\left(\frac{\chi\varsigma}{\xi}\right)} + \frac{2\xi}{\chi} \times \frac{\varsigma\left[K_0\left(\frac{\chi}{\xi}\right)I_1\left(\frac{\chi\varsigma}{\xi}\right) + I_0\left(\frac{\chi}{\xi}\right)K_1\left(\frac{\chi\varsigma}{\xi}\right)\right] + \left[I_1\left(\frac{\chi}{\xi}\right)K_0\left(\frac{\chi\varsigma}{\xi}\right) + K_1\left(\frac{\chi}{\xi}\right)I_0\left(\frac{\chi\varsigma}{\xi}\right)\right]}{K_0\left(\frac{\chi}{\xi}\right)I_0\left(\frac{\chi\varsigma}{\xi}\right) - I_0\left(\frac{\chi}{\xi}\right)K_0\left(\frac{\chi\varsigma}{\xi}\right)}\right\}\,. \tag{24}$$

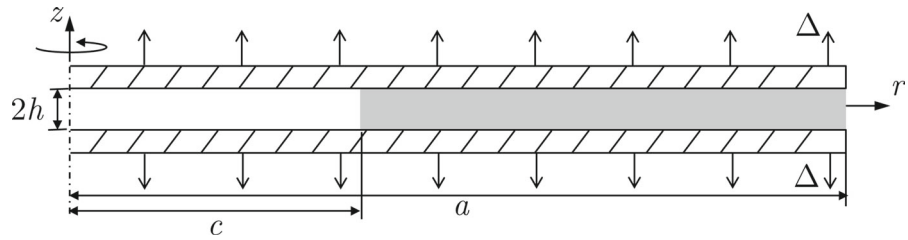

Fig. 4 An annular thin layer with $c \le r \le a$, used as an approximation for a thin layer containing a large axisymmetric crack of radius c

In this equation, we have reversed to the use of ξ and χ, but it is worth mentioning that the expression inside the curly brackets can be written using ς and ζ rather than ς, ξ, and χ.

Once combined, Eqs. (9), (18), and (24) yield

$$g_l^e(\xi,\chi,\varsigma) = \frac{3}{\chi^2}\left[\frac{\frac{\xi}{\chi\varsigma} - K_0\left(\frac{\chi}{\xi}\right)I_1\left(\frac{\chi\varsigma}{\xi}\right) - I_0\left(\frac{\chi}{\xi}\right)K_1\left(\frac{\chi\varsigma}{\xi}\right)}{K_0\left(\frac{\chi}{\xi}\right)I_0\left(\frac{\chi\varsigma}{\xi}\right) - I_0\left(\frac{\chi}{\xi}\right)K_0\left(\frac{\chi\varsigma}{\xi}\right)}\right]^2 \quad (25)$$

Note that this expression can be used to calculate $\tilde{g}_l^e$ in Eq. (21) by evaluating the limit of g_l^e as $\chi \to 0$.

The accuracy of the functions g_l^e, $\tilde{g}_l^e$, and $\bar{g}_l^e$ is assessed in Fig. 5 by comparing them with the corresponding finite element solutions for the normalized energy release rate. In Figs. 5a,c,e, we plot the energy release rate, normalized according to Eq. (9), versus $\varsigma = c/a$ for $\xi = 1/100, 1/50, 1/10$, respectively. In each of these plots, the analytical solutions, g_l^e, $\tilde{g}_l^e$, and $\bar{g}_l^e$, are shown as lines, while the finite element solutions are shown as discrete symbols. The function g_l^e in Eq. (25) is used for the NIM1 and NIM2 layers, the function $\tilde{g}_l^e$ in Eq. (21) is used for the IM layers, and the function $\bar{g}_l^e$ in Eq. (23) is used for the CM layers. As in Fig. 3, we also plot the relative errors in Figs. 5b,d,f.

The domains of validity of the approximate analytical solutions are colored green in Fig. 5. Within these domains, both c and $a - c$ are at least $10h$. Note that such a domain cannot be identified in Figs. 5e,f for the layers characterized by $\xi = 1/10$. In this case, the approximate analytical solutions are inaccurate and have relatively large errors. Within the domains of validity in Figs. 5a,c, the approximate analytical solutions compare well with the finite element solutions for $\xi = 1/100$ and $1/50$. The relative errors are around 1% or less for the CM layers. For the NIM1, NIM2, and IM layers, the errors are larger, but the overall trend is well captured by the approximate analytical solutions. Therefore, the approximate analytical solutions, g_l^e, $\tilde{g}_l^e$, and $\bar{g}_l^e$ in Eqs. (25), (21) and (23), respectively, are accurate for large cracks in sufficiently thin layers.

2.4 Summary of Solutions

The approximate analytical solutions for the normalized energy release rate, Eqs. (12), (13), and (14) for small cracks and Eqs. (21), (23), and (25) for large cracks, work well in their respective domains of validity. Here, we combine these solutions with their finite element counterparts and focus on their predictive capabilities in the entire parametric range. To this end, it is useful to rewrite Eqs. (12), (13), and (14) by replacing c/h with ς/ξ so that the three functions become

$$g_s^e(\xi,\chi,\varsigma) = \frac{27\varsigma}{4\pi\chi^4(3-\chi^2)\xi} \times \left\{2 + \frac{4\chi^6 - 24\chi^4 + 39\chi^2 - 18}{(3-\chi^2)\left[3I_0\left(\frac{\chi}{\xi}\right) - 2\xi\chi I_1\left(\frac{\chi}{\xi}\right)\right]}\right\}^2, \quad (26)$$

$$\tilde{g}_s^e(\xi,\varsigma) = \frac{9\varsigma}{16\pi\xi^5}, \quad (27)$$

and

$$\bar{g}_s^e(\xi,\chi,\varsigma) = \frac{27\varsigma}{\pi\chi^4(3-\chi^2)\xi}. \quad (28)$$

As a result, all of the six approximate analytical solutions, g_s^e, $\tilde{g}_s^e$, $\bar{g}_s^e$, g_l^e, $\tilde{g}_l^e$, $\bar{g}_l^e$ are expressed as functions of ξ, χ, and ς.

We summarize the six approximate analytical solutions developed in this section in Table 2. In all cases, the layer is assumed to be thin, that is, $\xi \ll 1$. The material is assumed to be linearly elastic, but can be compressible, nearly incompressible or incompressible, depending on the parameter χ. However, the layer compressibility depends on the ratio ξ/χ. For small cracks, the function $g_s^e(\xi,\chi,\varsigma)$ is applicable for all three cases, but can be simplified to $\bar{g}_s^e(\xi,\chi,\varsigma)$ if the layer is compressible or $\tilde{g}_s^e(\xi,\varsigma)$ if it is incompressible. For large cracks, the function $g_l^e(\xi,\chi,\varsigma)$ is applicable for nearly incompressible layers, but can be simplified to $\tilde{g}_l^e(\xi,\varsigma)$ as the incompressible limit. A more general solution for large cracks is too complicated to be useful.

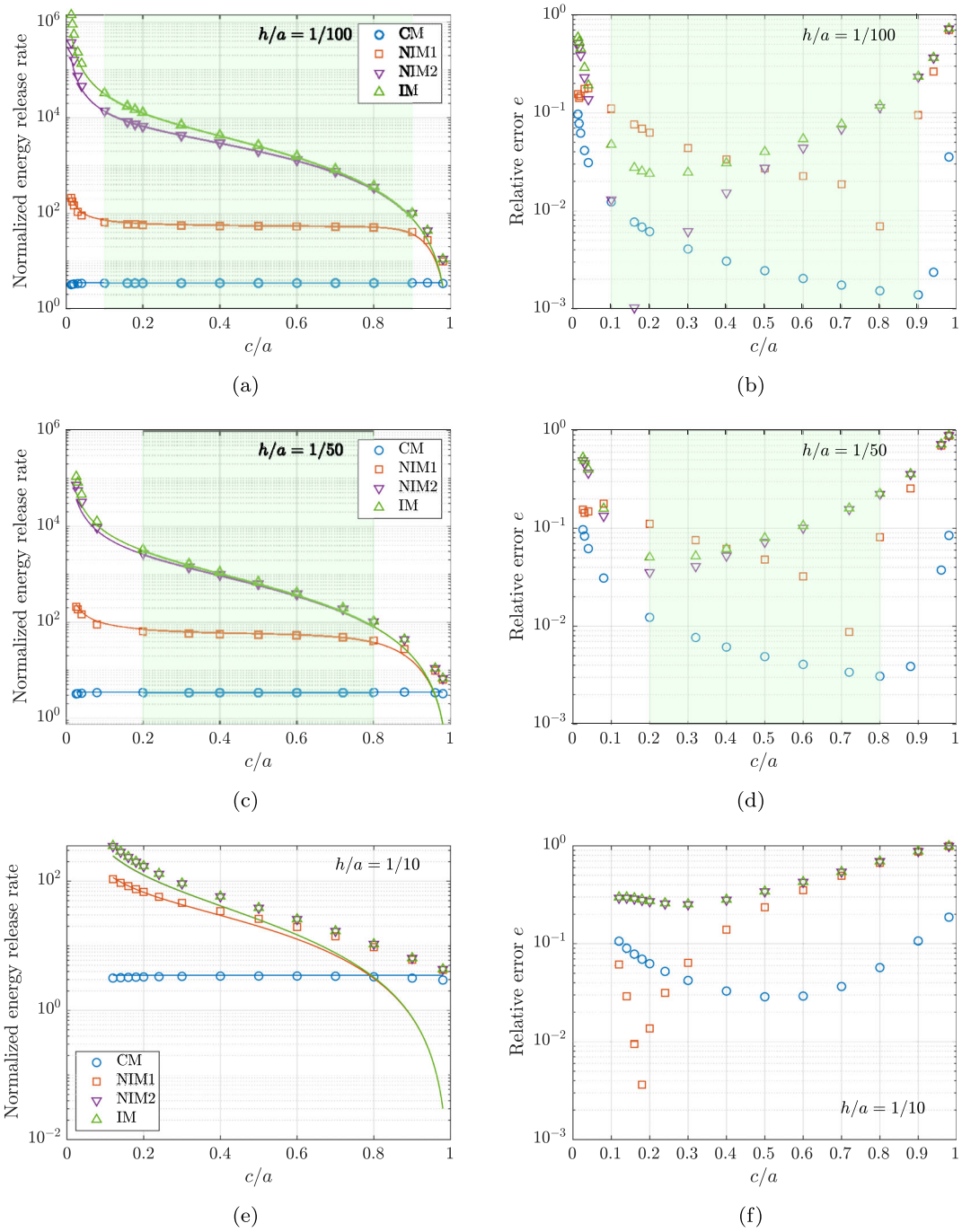

Fig. 5 The approximate analytical (lines) and finite element (symbols) solutions for large embedded cracks. (a,c,e) The energy release rate, normalized according to Eq. (9), versus c/a; (b,d,f) the relative error e of the approximate analytical solutions vis-à-vis finite element solutions versus c/a. The plots are paired so that $h/a = 1/100$ for (a,b), $h/a = 1/50$ for (c,d), and $h/a = 1/10$ for (e,f). In each plot, the approximate analytical solutions are represented by g_l^e for the NIM1 and NIM2 layers, by $\tilde{g}_l^e$ for the IM layers, and by $\bar{g}_l^e$ for the CM layers. These functions are specified in Eqs. (25), (21), and (23), respectively. The compressibility of the four materials, CM, NIM1, NIM2, and IM, are specified in Table 1. The domains of validity of the approximate analytical solutions are colored green

Table 2 Summary of the approximate analytical solutions for small and large embedded cracks in thin layers of various compressibility. All solutions are for $\xi \ll 1$

Layer compressibility	Small crack $\varsigma \ll \xi$	Large crack $\xi \ll \varsigma, 1-\varsigma$
Compressible $\xi/\chi \ll 1$	$\bar{g}_s^e(\xi, \chi, \varsigma)$	$\bar{g}_l^e(\chi)$
Nearly incompressible $\xi/\chi = \mathcal{O}(1)$	$g_s^e(\xi, \chi, \varsigma)$	$g_l^e(\xi, \chi, \varsigma)$
Incompressible $\xi/\chi \gg 1$	$\tilde{g}_s^e(\xi, \varsigma)$	$\tilde{g}_l^e(\xi, \varsigma)$

In Fig. 6, we present log-log plots for the normalized energy release rate by treating ξ and χ as parameters and ς as an argument. The values for ξ and χ are the same as in Figs. 3 and 5. Also, as in those two figures, we identify the domains of validity, where the approximate analytical solutions are expected to be accurate. Apparently, in all cases, the combined approximate analytical solutions are qualitatively in agreement with the finite element solutions for all crack sizes ($0 < \varsigma < 1$). Consequently, one can use the approximate analytical solutions for qualitative analysis not only for small and large cracks, but also for intermediate cracks. This is quite remarkable, as the approximate analytical solutions are not expected to be accurate there.

Three features of the plots in Fig. 6 are worth mentioning:

- For the CM layers, $\bar{g}^e$ increases linearly with c/a until it reaches a plateau, consistent with Eqs. (28) and (23). Note that $\bar{g}_l^e$ depends on χ only. That is, this function is geometry-independent.
- For the NIM1 and NIM2 layers, g^e first increases linearly with c/a and then decreases. This behavior is similar to $\tilde{g}^e$ for the IM layers, but is different from $\bar{g}^e$ for the CM layers. These similarities and differences are central to stability of crack growth discussed in Sect. 3.
- For fixed c/a and h/a, the normalized energy release rate increases considerably (by orders of magnitude) as the material compressibility χ decreases for the NIM layers, with an upper bound set by $\tilde{g}^e$ for the IM layers.

3 Stability of crack growth

In this section, we examine stability of growing axisymmetric embedded cracks in constrained thin layers, with the emphasis on the roles of the layer thinness ξ and material compressibility χ. We follow the traditional approach and consider both displacement- and force-controlled boundary conditions. The former represents situations involving loading devices whose stiffness is much larger than that of the specimen, whereas the latter represents situations involving loading devices whose stiffness is much smaller than that of the specimen. We aim to develop a qualitative understanding of the problem, based largely on the approximate analytical solutions in Sect. 2. Our stability analysis does not account for the R-curve effect (Kanninen and Popelar 1985), and it is restricted to examining the sign of the partial derivative, $\partial_c G := \partial G/\partial c$.

3.1 Displacement-controlled boundary conditions

Under displacement-controlled boundary conditions, it is natural to rely on Eq. (9) as the point of departure and evaluate $\partial_c G$ focusing on the normalized partial derivative, $\partial_\varsigma g := \partial g/\partial \varsigma$. Then, crack growth is stable if $\partial_\varsigma g < 0$, unstable if $\partial_\varsigma g > 0$, and neutral (or steady state) if $\partial_\varsigma g = 0$. These properties can be examined by inspecting Fig. 6. Accordingly, small cracks, characterized by $\varsigma \ll \xi$, are always unstable as $\partial_\varsigma g_s^e > 0$ for all ξ and χ. As ς increases, the normalized energy release rate g^e reaches a cross-over point and two distinct scenarios appear. For the CM layers, the cross-over signifies a transition from unstable to steady-state crack growth. In contrast, for the NIM1, NIM2, and IM layers, the cross-over signifies a transition from unstable to stable crack growth. That is, at a fixed Δ, a growing crack can be arrested if the layer is incompressible or nearly incompressible. This behavior is consistent with experimental observations of crack growth and arrest in rubber and PDMS layers (Gent and Lindley 1959; Guo and Ravi-Chandar 2023).

The results presented in Fig. 6 suggest that the normalized energy release rate for the NIM1 and NIM2 layers is qualitatively similar to that for the IM lay-

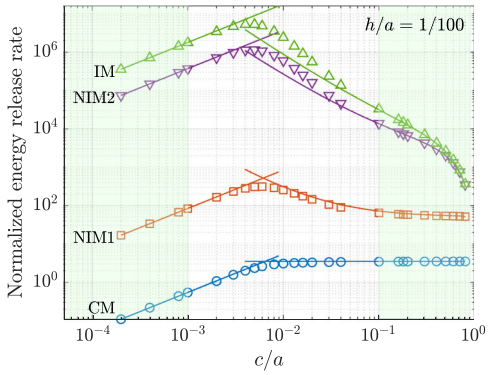

(a)

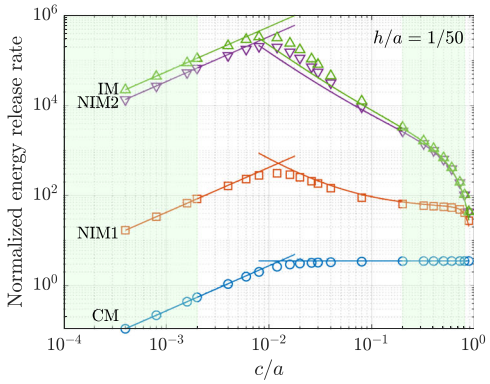

(b)

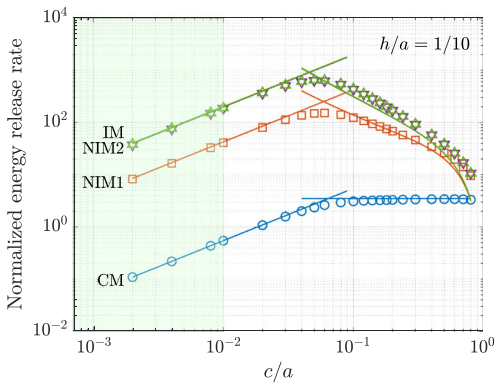

(c)

Fig. 6 The approximate analytical (lines) and finite element (symbols) solutions for embedded cracks. The energy release rate, normalized according to Eq. (9), versus c/a for: **a** $h/a = 1/100$, **b** $h/a = 1/50$, and **c** $h/a = 1/10$. In each plot, the approximate analytical solutions are represented by g_s^e and g_l^e for the NIM1 and NIM2 layers, by $\tilde{g}_s^e$ and $\tilde{g}_l^e$ for the IM layers, and by $\bar{g}_s^e$ and $\bar{g}_l^e$ for the CM layers. These pairs of functions are specified in Eqs. (26) and (25), (27) and (21), and (28) and (23), respectively. The compressibility of the four materials, CM, NIM1, NIM2, and IM, are specified in Table 1. The domains of validity of the approximate analytical solutions are colored green

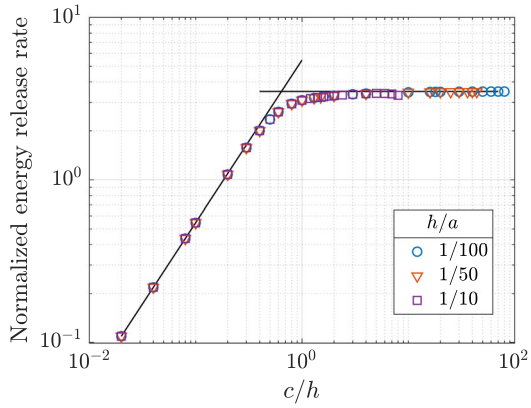

Fig. 7 The normalized energy release rate for axisymmetric embedded cracks in the CM layers ($\nu = 0.3$) versus c/h under displacement-controlled boundary conditions. The approximate analytical solutions, $\bar{g}_s^e$ and $\bar{g}_l^e$ (lines), viz-ã-viz the finite element solutions (symbols) are shown for three values of h/a

ers. Thus, for qualitative analysis, it is sufficient to use the functions $\tilde{g}_s^e$ and $\tilde{g}_l^e$ for incompressible and nearly incompressible layers. Similarly, for compressible layers, it is sufficient to use the functions $\bar{g}_s^e$ and $\bar{g}_l^e$. The two scenarios are discussed separately in the following.

For the CM layers, the normalized crack radius $\bar{\varsigma}^*$ associated with the transition from unstable to steady-state crack growth is determined approximately by setting

$$\bar{g}_s^e(\xi, \chi, \varsigma) = \bar{g}_l^e(\chi) \ . \tag{29}$$

Then, Eqs. (28) and (23) combine to yield

$$\bar{\varsigma}^* = \frac{\pi}{9}\chi^2\left(3 - \chi^2\right)\xi \ . \tag{30}$$

Thus, the transition occurs at a crack radius that is proportional to the thickness of the layer. For the CM layers with $\chi = 0.9258$, this equation yields $\bar{\varsigma}^* = 0.64\xi$ or $c^* = 0.64h$, which is consistent with the numerical results in Fig. 7.

Similarly, for the IM layers, the normalized crack radius $\tilde{\varsigma}^*$ associated with the transition from unstable to stable crack growth is determined approximated by setting

$$\tilde{g}_s^e(\xi, \varsigma) = \tilde{g}_l^e(\xi, \varsigma) \ . \tag{31}$$

Upon substitution of Eqs. (27) and (21) into Eq. (31), we obtain

$$\xi^3 = \frac{3\left(\tilde{\varsigma}^*\right)^3 \log^2 \tilde{\varsigma}^*}{\pi\left[1 - \left(\tilde{\varsigma}^*\right)^2 + 2\left(\tilde{\varsigma}^*\right)^2 \log \tilde{\varsigma}^*\right]^2} \ . \tag{32}$$

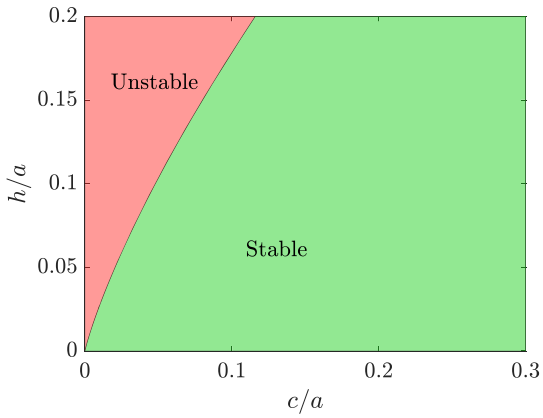

Fig. 8 The stability map for crack growth in the IM layers ($\nu = 0.5$) under displacement-controlled boundary conditions

This equation cannot be solved for $\tilde{\varsigma}^*$ explicitly. Nevertheless, it is sufficient for constructing the stability map shown in Fig. 8, where Eq. (32) sets the boundary between the regions of unstable and stable crack growth. This map clearly shows that stable crack growth is favored in thinner layers, and the transition crack size $\tilde{\varsigma}^*$ decreases as ξ decreases. Consequently, smaller cracks can be arrested in thinner layers. This is in agreement with experimental observations (Gent and Lindley 1959; Guo and Ravi-Chandar 2023).

3.2 Force-controlled boundary conditions

In general, crack growth under force-controlled boundary conditions is less stable than under displacement-controlled boundary conditions (Kanninen and Popelar 1985). To clarify this statement, let us consider two identical specimens, one subjected to force-controlled boundary conditions and the other to displacement-controlled boundary conditions. It can be shown that, if $G_{|F} = G_{|\Delta}$, then

$$\partial_c G_{|F} > \partial_c G_{|\Delta} \,. \tag{33}$$

This implies that, under force-controlled boundary conditions, $\partial_c G > 0$ for all crack sizes in compressible layers, and thus crack growth is always unstable. Therefore, there is no transition to be analyzed in this case. Following our analysis of displacement-controlled boundary conditions, stability of crack growth is qualitatively similar in incompressible and nearly incompressible layers. Consequently, in the remainder of this subsection, we focus on crack growth in incompressible layers under force-controlled boundary conditions.

Stability of crack growth under force-controlled conditions in incompressible layers is analyzed by rewriting the energy release rate G in terms of the applied force F rather than the displacement Δ. To this end, G is expressed as

$$\tilde{G}^e = \tilde{\gamma}^e\left(\xi, \varsigma\right) \times \mu a \left(\frac{F}{\pi a^2 \mu}\right)^2 , \tag{34}$$

where $\tilde{\gamma}^e$ is a dimensionless function.

For the IM layers, the force-elongation relations are given by Eqs. (A.15) and (20) for small and large cracks, respectively. Combining these relations with $\tilde{g}_s^e$ in Eq. (13) and $\tilde{g}_l^e$ in Eq. (21), we obtain

$$\tilde{\gamma}_s^e = \frac{4\varsigma}{\pi} \,, \tag{35}$$

and

$$\tilde{\gamma}_l^e = \frac{\xi^3}{3}\left\{\frac{2\left(1-\varsigma^2+2\varsigma^2\log\varsigma\right)}{\varsigma(1-\varsigma^2)\left[1-\varsigma^2+\left(1+\varsigma^2\right)\log\varsigma\right]}\right\}^2 \tag{36}$$

In Fig. 9, we compare the normalized energy release rates $\tilde{\gamma}_s^e$ in Eq. (35) and $\tilde{\gamma}_l^e$ in Eq. (36) with the corresponding finite element solutions. Note that $\tilde{\gamma}_s^e$ is independent of ξ, but $\tilde{\gamma}_l^e$ increases with ξ. Furthermore, $\tilde{\gamma}_s^e$ increases linearly with ς, while $\tilde{\gamma}_l^e$ depends on ς non-monotonically. Figure 9 shows that the approximate analytical solutions in Eqs. (35) and (36) are in qualitative agreement with the corresponding finite element solutions for values of ξ up to $1/10$. Thus, the approximate analytical solutions may be used for qualitative analyses of crack growth stability. In particular, we identify two transitions under force-controlled conditions: (i) from unstable to stable crack growth, and (ii) from stable back to unstable crack growth. The first transition is similar to that present under displacement-controlled boundary conditions, while the second transition is absent under displacement-controlled conditions. Qualitatively similar transitions were noted by Benvidi and Bacca (2021) for axisymmetric interfacial cracks.

The first transition point $\tilde{\varsigma}_1$ is determined by equating $\tilde{\gamma}_s^e$ and $\tilde{\gamma}_l^e$ in Eqs. (35) and (36), respectively. As a result, we obtain

$$\xi^3 = \frac{3\tilde{\varsigma}_1^3\left[\left(1-\tilde{\varsigma}_1^2\right)^2+\left(1-\tilde{\varsigma}_1^4\right)\log\tilde{\varsigma}_1\right]^2}{\pi\left(1-\tilde{\varsigma}_1^2+2\tilde{\varsigma}_1^2\log\tilde{\varsigma}_1\right)^2} \,. \tag{37}$$

This equation cannot be solved for $\tilde{\varsigma}_1$ explicitly.

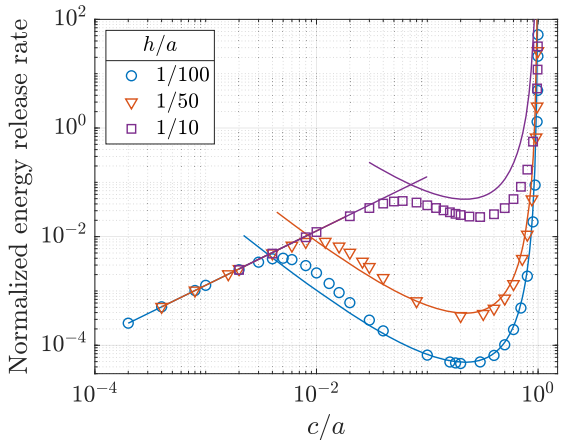

Fig. 9 The normalized energy release rate for axisymmetric embedded cracks in the IM layers ($\nu = 0.5$) versus c/a under force-controlled boundary conditions. The approximate analytical solutions, $\tilde{\gamma}_s^e$ and $\tilde{\gamma}_l^e$ (lines), viz-ã-viz the finite element solutions (symbols) are shown for three values of h/a

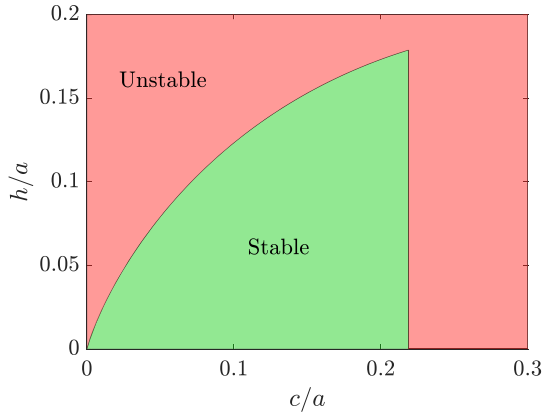

Fig. 10 The stability map for crack growth in IM layers ($\nu = 0.5$) under force-controlled boundary conditions

For the second transition point, $\tilde{\varsigma}_2$, we need to determine the minimum of $\tilde{\gamma}_l^e$. Upon differentiation of Eq. (36), we obtain

$$\tilde{\varsigma}_2 \approx 0.22\,. \tag{38}$$

Thus, this transition is independent of ξ.

Equations (37) and (38) allow us to construct the stability map shown in Fig. 10, for crack growth in incompressible layers under force-controlled boundary conditions. On this map, the curved boundary corresponds to Eq. (37) and the first transition, whereas the vertical boundary corresponds to Eq. (38) and the second transition. The two boundaries intersect at a point with $\xi \approx 0.18$. Therefore, stable crack growth under force-controlled boundary conditions is possible only in thin layers with $\xi < 0.18$. Moreover, the range for stable crack growth increases as ξ decreases, but the largest stable crack size, $\varsigma \approx 0.22$ or $c \approx 0.22a$, is independent of ξ. The map in Fig. 10 clearly shows that stable crack growth is possible under force-controlled boundary conditions, provided that the layer is sufficiently thin and the material is nearly incompressible.

4 Axisymmetric problems for interfacial cracks

In this section, we analyze the problem identical to that analyzed in Sect. 2, but with one major exception, as the crack is no longer located in the mid-plane of the layer. Rather, its center is shifted along the z-axis to the interface between the layer and the lower rigid plate (Fig. 11a). Technical differences between analyzing the embedded and interfacial cracks are significant, but the strategy is the same. Therefore the flow in this section is similar to that in Sect. 2. In particular, once the supercript e, for embedded cracks, is replaced with i, for interfacial cracks, the functions summarized in Table 2 for the embedded cracks becomes their counterparts for the interfacial cracks.

For small cracks, $c \ll h \ll a$, the original problem (Fig. 11a) is equivalent to the problem for a crack of radius c at the interface between two semi-infinite bodies (Fig. 11b). The semi-infinite body above the crack is characterized by the elastic properties of the layer and the semi-infinite body below the crack is rigid. The upper crack face is subjected to the opening stress σ_1, which would be transmitted through the point $(r = 0, z = -h)$ if the layer were uncracked; see (A.13). There is no shear stress at this location due to axial symmetry.

The problem in Fig. 11b is analyzed in two steps: (i) by calculating the complex stress intensity factor of the crack, $K = K_1 + iK_2$ (Kassir and Bregman 1972; Rice 1988), and (ii) by expressing the energy release rate G_s^i in terms of K_1 and K_2 (Malyshev and Salganik 1965; Rice 1988; Hutchinson and Suo 1991). Here, we present our result using the widely accepted notation for interfacial cracks (Rice 1988; Hutchinson and Suo 1991) as opposed to that used in Malyshev and Salganik (1965) and Kassir and Bregman (1972).

For a circular interfacial crack between elastic and rigid semi-infinite bodies (Fig. 11b), the complex stress

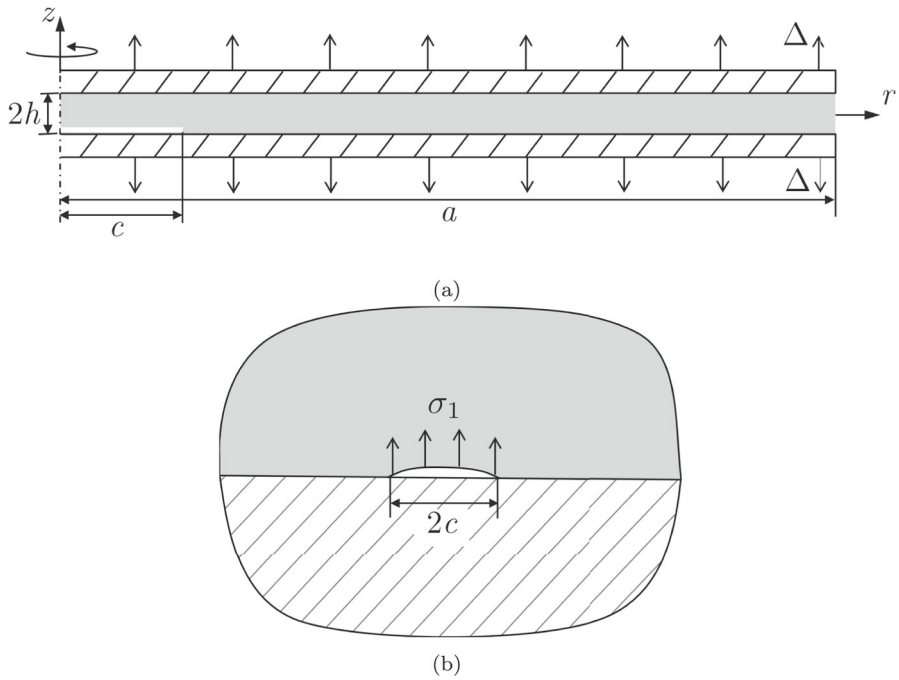

Fig. 11 **a** An axisymmetric interfacial crack between a constrained elastic layer and a rigid plate, and **b** an interfacial crack between two semi-infinite bodies subjected to the opening traction σ_1

intensity factor can be obtained from a more general solution by Kassir and Bregman (1972):

$$K = K_1 + iK_2 = 2\sigma_1\sqrt{c}\frac{\Gamma(2+i\varepsilon)}{\Gamma(1/2+i\varepsilon)}\,. \tag{39}$$

Here Γ is Euler's Γ-function (Abramowitz and Stegun 1968) and

$$\varepsilon = \frac{1}{2\pi}\log\frac{3+\chi^2}{3-\chi^2}\,. \tag{40}$$

Following Rice (1988) and Hutchinson and Suo (1991), the corresponding energy release rate for the interfacial crack is expressed as

$$G_s^i = \frac{3+\chi^2}{24\mu}\left(K_1^2 + K_2^2\right)\,. \tag{41}$$

Using Eq. (39) and the identities

$$\left|\Gamma\left(2+i\varepsilon\right)\right|^2 = \frac{\pi\varepsilon\left(1+\varepsilon^2\right)}{\sinh(\pi\varepsilon)} \quad \text{and}$$
$$\left|\Gamma\left(\frac{1}{2}+i\varepsilon\right)\right|^2 = \frac{\pi}{\cosh(\pi\varepsilon)}\,, \tag{42}$$

we specify Eq. (41) as

$$G_s^i = \frac{\left(3+\chi^2\right)\left(1+\varepsilon^2\right)\varepsilon}{2\mu\chi^2}\sigma_1^2 c\,. \tag{43}$$

This expression differs from Eq. (8) in Benvidi and Bacca (2021), also derived from the solution of Kassir and Bregman (1972). The two analytical solutions are identical only if the material is incompressible. Besides cosmetic differences, associated with the use of the standard elastic constants E and ν, there are two typos in Benvidi and Bacca (2021). First, in Eq. (5), leading to Eq. (8), the denominator must be $E^*\cosh^2(\pi\varepsilon)$ rather than $E^*\cosh(\pi\varepsilon)$, and this typo persists in Eq. (8). Second, in Eq. (8), it must be $\Gamma(2+i\varepsilon)$ rather than $\Gamma(1+i\varepsilon)$, according to Kassir and Bregman (1972). In addition, the inclusion of the term $(2\hat{c})^{i\varepsilon}$ in Eq. (8) is unnecessary because its magnitude is one.

For a small interfacial crack in a constrained thin layer (Fig. 11a), the energy release rate is obtained by substituting Eq. (A.13) for the stress σ_1 in Eq. (43). Following Eq. (9), the normalized energy release rate is

$$g_s^i(\xi,\chi,\varsigma) = \frac{9\left(3+\chi^2\right)\left(1+\varepsilon^2\right)\varepsilon}{2\chi^6} \times\left\{1+\frac{9-6\chi^2}{\left(3-\chi^2\right)\left[2\xi\chi I_1\left(\frac{\chi}{\xi}\right)-3I_0\left(\frac{\chi}{\xi}\right)\right]}\right\}^2\left(\frac{\varsigma}{\xi}\right)\,. \tag{44}$$

Further, following Eqs. (13) and (14), we obtain

$$\tilde{g}_s^i(\xi,\varsigma) = \frac{9\varsigma}{32\pi\xi^5} \tag{45}$$

and

$$\bar{g}_s^i(\xi,\chi,\varsigma) = \frac{9\left(3+\chi^2\right)\left(1+\varepsilon^2\right)\varepsilon}{2\chi^6}\left(\frac{\varsigma}{\xi}\right), \tag{46}$$

respectively. Note that Eq. (44) is valid for all values of χ, while Eq. (45) is valid for $\xi/\chi \gg 1$ and Eq. (46) for $\xi/\chi \ll 1$.

Let us mention that our approach above differs from that in Benvidi and Bacca (2021). First, as illustrated in Fig. 11, we assume the displacement-controlled condition and thus normalize the energy release rate according to Eq. (9), whereas Benvidi and Bacca (2021) assumed a uniform remote stress applied to the rigid plates and normalized the energy release rate in a way similar to Eq. (34) under the force-controlled condition. Second, Benvidi and Bacca (2021) focused on the cases with nearly incompressible materials and assumed $\varepsilon \approx 0$ to simplify the analytical solution. Here, Eq. (44) is valid for all material compressibility, with two limits for incompressible and compressible layers in Eqs. (45) and (46), respectively. Third, in our analysis, the stress σ_1 in Eq. (43) is obtained from the asymptotic solution for uncracked layers (Appendix A), while the local stress in Benvidi and Bacca (2021) was obtained from finite element analysis of uncracked layers.

For large interfacial cracks, $c \gg h$ and $a - c \gg h$, we retain the underlying assumption for the approximate analytical solutions for large embedded cracks, and therefore

$$g_l^i(\xi,\chi,\varsigma) = g_l^e(\xi,\chi,\varsigma), \quad \tilde{g}_l^i(\xi,\varsigma) = \tilde{g}_l^e(\xi,\varsigma), \quad \text{and} \quad \bar{g}_l^i(\chi) = \bar{g}_l^e(\chi); \tag{47}$$

see Eqs. (21), (23), and (25) for details.

The accuracy of the approximate analytical solutions for interfacial cracks is assessed by comparing them with the corresponding finite element solutions. The finite element mesh used for the interfacial crack is similar to that in Fig. 2, except that the entire elastic layer is meshed, with the Dirichlet boundary condition ahead of the crack. The energy release rate for the interfacial crack is computed by evaluating the J-integral over the semicircular contours in the elastic layer. Similarly to those for embedded cracks, the approximate analytical solutions are reasonably accurate within their domains of validity. Figure 12, patterned after Fig. 6, shows both analytical and finite element solutions versus ς. That is, each plot is for a fixed ξ, containing solutions for both small and large cracks for the CM, NIM1 and NIM2, and IM layers. In addition, the domains of validity in Fig. 12 are the same as in Fig. 6. The parallels between the two figures include not only their organization, but also the results, which appear to be very similar, at least qualitatively. For this reason, comments pertaining to Fig. 6, made at the end of Section 2.4, are also applicable to Fig. 12.

5 Embedded versus interfacial cracks

It is natural to compare the embedded versus interfacial cracks by evaluating the ratio

$$\rho(\xi,\chi,\varsigma) := \frac{g^i(\xi,\chi,\varsigma)}{g^e(\xi,\chi,\varsigma)}, \tag{48}$$

where g^i and g^e are the normalized energy release rates of the interfacial and embedded cracks, respectively. For both small and large cracks, this ratio is independent of the crack size. In particular, according to Eq. (47), for large cracks ($\xi \ll \varsigma, 1-\varsigma$), we have

$$\rho_l = \tilde{\rho}_l = \bar{\rho}_l = 1. \tag{49}$$

For small cracks ($\varsigma \ll \xi$), the ratio ρ_s can be calculated from the approximate analytical solutions in Eqs. (12) and (44). Alternatively, according to Eqs. (13) and (45), for incompressible layers ($\xi/\chi \gg 1$), we obtain

$$\tilde{\rho}_s = \frac{1}{2}. \tag{50}$$

For compressible layers ($\xi/\chi \ll 1$), Eqs. (14) and (46) yield

$$\bar{\rho}_s(\chi) = \frac{(9-\chi^4)\left(1+\varepsilon^2\right)}{12\chi^2}\log\frac{3+\chi^2}{3-\chi^2}. \tag{51}$$

Figure 12 shows the ratio $\bar{\rho}_s$ viz-à-viz finite element results as a function of χ for $\xi = 1/100, 1/50$ and $1/10$. The agreement is excellent for the two thinner layers ($\xi = 1/100$ and $1/50$), but not so for the thicker layer ($\xi = 1/10$). This is expected as the approximate analytical solutions are accurate only for thin layers. Interestingly, for both compressible and incompressible layers, the ratios $\bar{\rho}_s$ and $\tilde{\rho}_s$ are independent of ξ. However, for nearly incompressible layers ($\xi/\chi = \mathcal{O}(1)$), the ratio ρ_s is approximately $1/2$, but decreases slightly as ξ increases. Thus, the energy release rate for an interfacial crack is approximately one-half that of an embedded crack of the same size, as has been noted by others (Crosby et al. 2000).

As the crack size increases from small to large, the ratio $\rho(\xi,\chi,\varsigma)$ transitions from approximately one

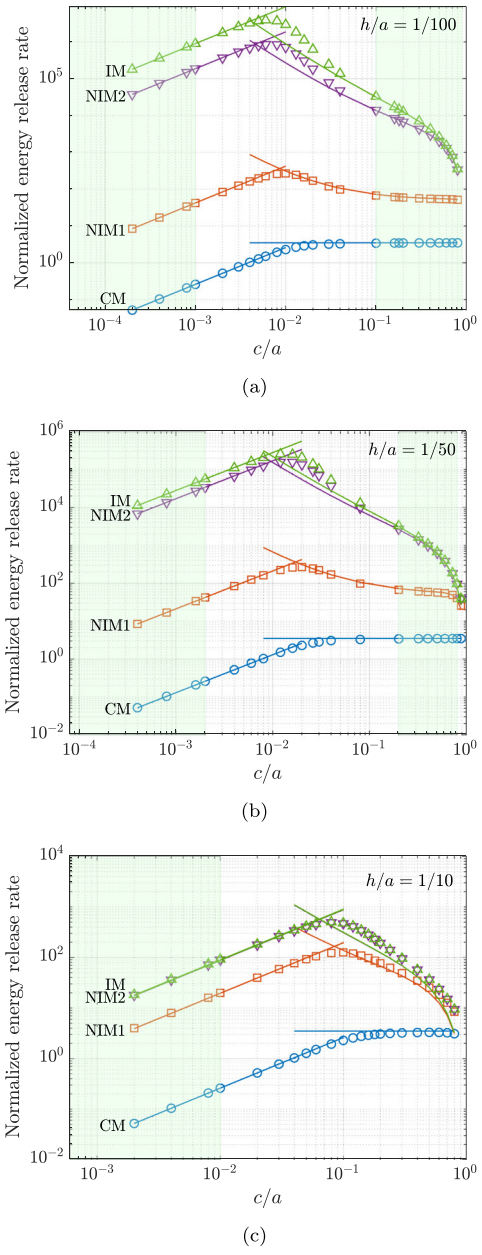

Fig. 12 The approximate analytical (lines) and finite element (symbols) solutions for interfacial cracks. The energy release rate, normalized according to Eq. (9), versus c/a: **a** $h/a = 1/100$, **b** $h/a = 1/50$, and **c** $h/a = 1/10$. In each plot, the approximate analytical solutions are represented by g_s^i and g_l^i for the NIM1 and NIM2 layers, by $\tilde{g}_s^i$ and $\tilde{g}_l^i$ for the IM layers, and by $\bar{g}_s^i$ and $\bar{g}_l^i$ for the CM layers. These pairs of functions are specified in Eqs. (44) and (25), (45) and (21), and (46) and (23), respectively. The compressibility of the four materials, CM, NIM1, NIM2, and IM, are specified in Table 1. The domains of validity of the approximate analytical solutions are colored green

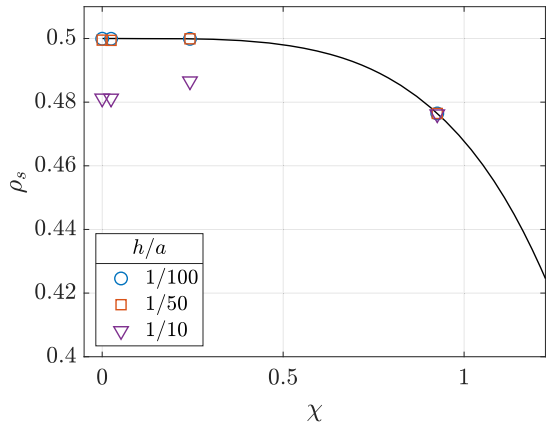

Fig. 13 The ratio of the normalized energy release rates for small interfacial/embedded cracks, ρ_s, versus the compressibility parameter χ, comparing Eq. (51) (line) and the finite element results (symbols) for three different values of h/a

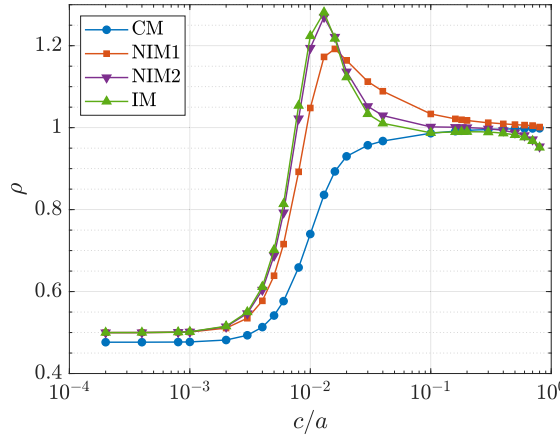

Fig. 14 The ratio of the normalized energy release rates, $\rho = g^i/g^e$, versus the normalized crack size c/a for $h/a = 1/100$, obtained by finite element analysis. The compressibility of the four materials, CM, NIM1, NIM2, and IM, are specified in Table 1

half when $\varsigma \ll \xi$ to one when $\xi \ll \varsigma, 1-\varsigma$. Figure 14 shows this transition based on finite element solutions for $\xi = 1/100$. Note that $\rho(\xi, \chi, \varsigma)$ is a monotonic function of the normalized crack size ς for the CM layers, but not monotonic for the IM and NIM layers.

In this work, the focus has been on axisymmetric planar cracks lying in the mid-plane or the interfaces. These configurations are the extreme cases for planar cracks lying in planes $z = z_c$, with $|z_c| \leq h$. The energy release rate for these intermediate configurations is expected to vary between the two extremes. This assertion has been confirmed by analyzing two numer-

ical examples, one for a small crack and the other for a large crack. However, an example involving an intermediate crack size revealed a more complex behavior, which deserves a separate study.

6 Non-axisymmetric problems

In this section, we restrict our attention to planar cracks in compressible layers ($\xi/\chi \ll 1$), but without insisting on axial symmetry. Thus, the layer and crack platforms are no longer required to be concentric circles. In fact, their shapes can be essentially arbitrary. This extension is based on the asymptotic analysis in Movchan et al. (2023), which applies only to compressible layers.

6.1 Background

Consider the class of problems stated in Sects. 2 and 4, but without insisting on axial symmetry. That is, neither the layer nor the crack front is required to be circular and aligned. Rather, the layer and crack platforms are defined by smooth planar curves, Γ_L and Γ_C, respectively (Fig. 15). This generalization requires us to reformulate the definitions of thin layers, small cracks, and large cracks. To this end, we identify the smallest circle containing Γ_L and denote it by $\bar{\Gamma}_L$. We adopt the radius of $\bar{\Gamma}_L$ as the effective radius of the layer and denote it by a. Similarly, we identify the smallest circle containing Γ_C and denote it by $\bar{\Gamma}_C$. We adopt the radius of $\bar{\Gamma}_C$ as the effective radius of the crack and denote it by c. Of course, if Γ_L and Γ_C are concentric circles, the new definitions recover those of the axisymmetric problem. With these definitions, thin layers are defined by the inequality $h \ll a$, and small cracks are defined by the inequality $c \ll h$. To define large cracks, let us identify two points

$$(x_C, y_C) \in \Gamma_C \quad \text{and} \quad (x_L, y_L) \in \Gamma_L \,.$$

The shortest distance between Γ_C and Γ_L is defined as

$$\begin{aligned} d &:= \text{distance}\,(\Gamma_C, \Gamma_L) \\ &:= \min \sqrt{(x_C - x_L)^2 + (y_C - y_L)^2}\,, \end{aligned} \tag{52}$$

where the minimum is evaluated over all pairs of points, one belonging to Γ_C and the other to Γ_L (Fig. 15). We regard d as the smallest ligament size ahead of the crack, so that large cracks are defined by the inequalities

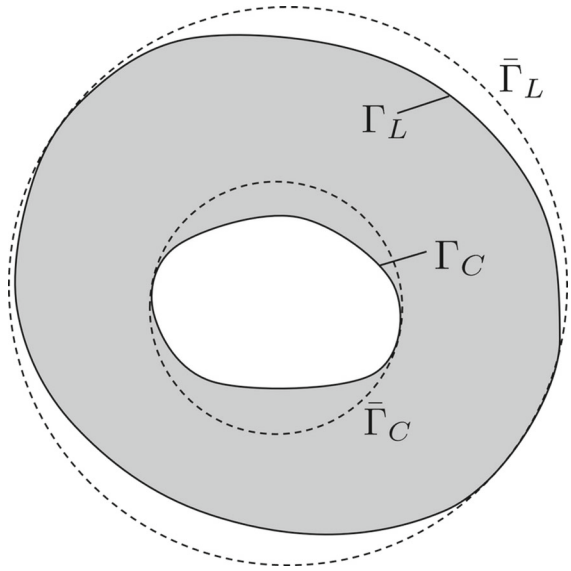

Fig. 15 Schematic of a non-axisymmetric problem, with a planar crack front Γ_c lying in the mid-plane of a layer bounded by Γ_L. The smallest circle containing Γ_C is $\bar{\Gamma}_C$, and the smallest circle containing Γ_L is $\bar{\Gamma}_L$

$c \gg h$ and $d \gg h$. Again, this definition of large cracks is consistent with that for the axisymmetric problem.

Our approach to the non-axisymmetric problem is based on the asymptotic analysis of Movchan et al. (2023), where it is shown that the displacements in the bulk of a compressible layer (except for small regions near the edges) are

$$u_z = \Delta \frac{z}{h}, \quad u_x = u_y = 0\,, \tag{53}$$

regardless of the shape of the layer. Here the x-axis and y-axis must form a right-handed Cartesian system with the z-axis, but arbitrary otherwise. The stresses corresponding to Eq. (53) are

$$\begin{aligned} &\sigma_{zz} = \frac{3\mu\Delta}{\chi^2 h}, \quad \sigma_{xx} = \sigma_{yy} = \frac{\left(3 - 2\chi^2\right)\mu\Delta}{\chi^2 h}, \quad \text{and} \\ &\sigma_{xy} = \sigma_{xz} = \sigma_{yz} = 0\,, \end{aligned} \tag{54}$$

and the strain energy density is

$$w = \frac{3\mu}{2\chi^2}\left(\frac{\Delta}{h}\right)^2 . \tag{55}$$

Therefore, the stress field is uniform in the bulk of the layer (except for small regions near the edges), which allows the analysis of non-axisymmetric problems in this section. However, the same analysis does not apply for incompressible or nearly incompressible layers, where the stress field in the bulk is not uniform.

The asymptotic analysis of thin layers with non-circular platforms requires additional assumptions, necessary to guarantee exponentially decaying edge effects (Movchan et al. 2023). Consequently, we assume that the smallest radius of curvature of Γ_L is much larger than h. In addition, for large cracks, the radius of curvature of Γ_C is also much larger than h. For small cracks, the shape of Γ_C can be arbitrary but smooth.

6.2 Small embedded cracks

In the absence of axial symmetry, the energy release rate for a small embedded crack can be obtained by modifying Eq. (10) as follows. First, for compressible layers, Eq. (A.12) is simplified as in Eq. (54) so that

$$\sigma_0 = \frac{3\mu}{\chi^2}\frac{\Delta}{h}\,. \tag{56}$$

Second, the expression for the stress intensity factor K_I is modified by taking into account that it depends on the location along Γ_C but not on elastic constants (Mear and Rodin 2011):

$$K_I = \frac{2}{\pi}\varphi\,(p)\,\sigma_0\sqrt{\pi c}\,. \tag{57}$$

Here φ is a function specific to Γ_C and p is a variable parameterizing the crack front Γ_C. Upon combining Eqs. (56) and (57) we obtain the generalization of Eq. (14) for non-axisymmetric small cracks:

$$\bar{g}_s^e\left(\chi, \frac{c}{h}, p\right) = \varphi^2\,(p)\,\frac{27}{\pi\chi^4\left(3-\chi^2\right)}\left(\frac{c}{h}\right)\,. \tag{58}$$

The only difference between this equation versus Eq. (14) is the factor $\varphi^2\,(p)$, which depends on the shape of the crack front Γ_C.

6.3 Large embedded cracks

Following Sect. 2.3, for large embedded cracks, we calculate the potential energy as the strain energy stored in the ligament ahead of the crack front. For an annular layer, Eq. (55) implies

$$P_l = [2h\,(A_L - A_C)]\,w = \frac{3\,(A_L - A_C)}{\chi^2} \times\mu h\left(\frac{\Delta}{h}\right)^2\,. \tag{59}$$

Here A_L and A_C are the areas enclosed by Γ_L and Γ_C, respectively, and the term in square brackets is the volume of the ligament ahead of the crack front. The energy release rate follows immediately from Eq. (59):

$$\bar{G}_l^e = -\frac{\partial P_l}{\partial A_C} = \frac{3}{\chi^2}\times\mu h\left(\frac{\Delta}{h}\right)^2\,, \tag{60}$$

and consequently

$$\bar{g}_l^e = \frac{3}{\chi^2}\,. \tag{61}$$

Remarkably, this result coincides with $\bar{g}_l^e$ in Eq. (23) for axi-symmetric large cracks. Thus, the energy release rate for large cracks embedded in compressible layers is independent of details of either Γ_C or Γ_L, as long as the contours are smooth and the smallest radius of curvature is much larger than h.

6.4 Elliptical embedded cracks

As an example, consider embedded elliptical cracks. Since there is an exact analytical solution for the stress intensity factor of an elliptical crack embedded in an infinite solid, this solution can be used to construct the function $\varphi(p)$ in Eq. (57). The solution can be found in Tada et al. (1973), and it can be traced back to Sadowsky and Sternberg (1949), Green and Sneddon (1950), and Irwin (1962). In particular, for an elliptical crack with the long semi-axis c and short semi-axis αc ($0 < \alpha \leq 1$), the stress intensity factor is

$$K_I = \frac{\sqrt{\alpha}\left(\sin^2\theta + \alpha^2\cos^2\theta\right)^{1/4}}{E(\alpha)}\sigma_0\sqrt{\pi c}\,. \tag{62}$$

Here $E(\alpha)$ is the complete elliptic integral of the second kind (Abramowitz and Stegun 1968) and θ is the angle that parameterize the elliptical crack front (Fig. 16) such that the coordinates of each point on the crack front are:

$$x = c\cos\theta \quad \text{and} \quad y = \alpha c\sin\theta\,.$$

Upon comparing Eqs. (57) and (62), we obtain

$$\varphi(\theta) = \frac{\pi\sqrt{\alpha}\left(\sin^2\theta + \alpha^2\cos^2\theta\right)^{1/4}}{2E(\alpha)}\,. \tag{63}$$

Substituting Eq. (63) into Eq. (58), we obtain

$$\bar{g}_s^e\left(\chi, \frac{c}{h}, \theta\right) = \frac{27\pi\alpha\sqrt{\sin^2\theta + \alpha^2\cos^2\theta}}{4\chi^4\left(3-\chi^2\right)E^2(\alpha)}\left(\frac{c}{h}\right)\,. \tag{64}$$

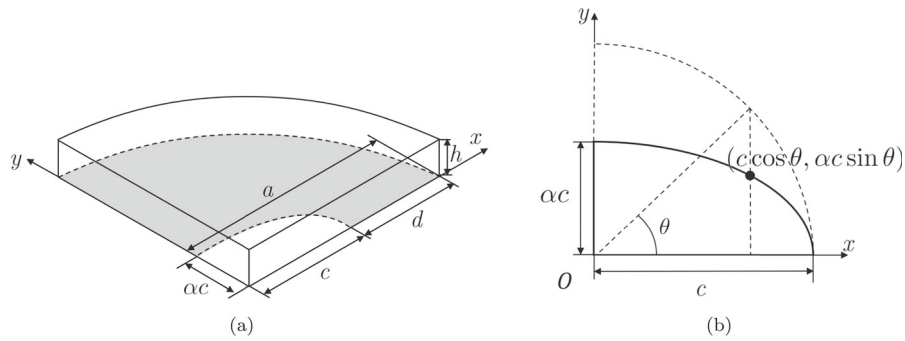

Fig. 16 Schematic of an elliptical crack in a thin layer (showing a quarter of the crack front only), and the parametrization of an elliptical crack front by the angle θ

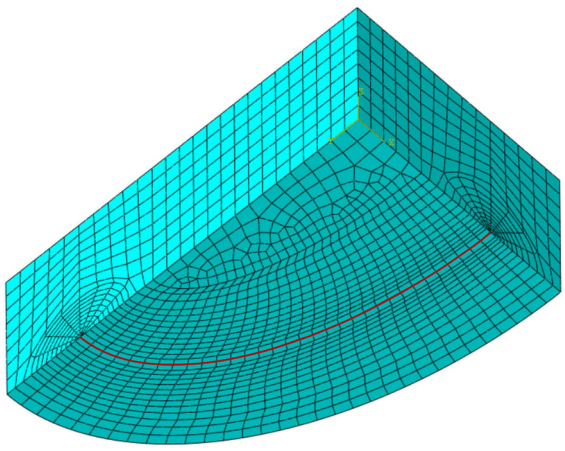

Fig. 17 A 3D finite element mesh for the region near an elliptical crack front (indicated by the red line). Only a quarter of the crack front is shown

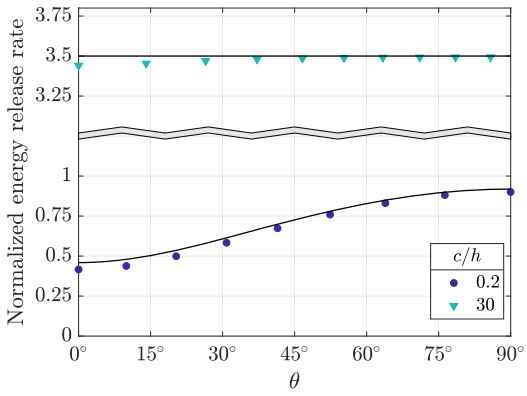

Fig. 18 The normalized energy release rate along the front of a small ($c/h = 0.2$) and a large ($c/h = 30$) embedded elliptical cracks ($\alpha = 0.5$), versus the angle θ. The analytical solutions, $\bar{g}_s^e$ in Eq. (64) and $\bar{g}_l^e$ in Eq. (61), are shown as lines, and the finite element solutions are shown as symbols. The CM layer is characterized by $\nu = 0.3$ and $\xi = 1/50$

Of course, for large elliptical cracks, $\bar{g}_l^e$ is shape independent and given by Eq. (61).

To assess the accuracy of the approximate analytical solutions, a 3D finite element mesh (Fig. 17) was constructed for an elliptical crack embedded in a CM layer characterized by $\nu = 0.3$ and $\xi = 1/50$. This mesh was formed by displacement-based quadratic elements (C3D20 and C3D15 in ABAQUS). The mesh parameters were chosen using the two-dimensional mesh in Fig. 2 as a guide. At each point along the crack front, we determined the energy release rate by calculating the J-integral in the plane normal to the crack front. The normalized energy release rate is then determined as a function of θ.

The approximate analytical solutions in Eqs. (61) and (64) are compared with the corresponding finite element solutions for a small ($c/h = 0.2$) and a large ($c/h = 30$) elliptical cracks. Both cracks are characterized by $\alpha = 0.5$ and are embedded in a CM layer characterized by $\xi = 1/50$. The comparisons are presented in Fig. 18, where Eqs. (61) and (64) are plotted as functions of θ for both cracks. It is clear that, in both cases, the approximate analytical and finite element solutions are in good agreement.

6.5 Interfacial cracks

In this subsection, we exploit the results for non-axisymmetric embedded cracks to develop approximate analytical solutions for non-axisymmetric interfacial cracks. As in the case of axisymmetric cracks, we retain the underlying assumption for large embedded and interfacial cracks, and therefore

$$\bar{g}_l^i = \bar{g}_l^e = \frac{3}{\chi^2}\,. \tag{65}$$

For small interfacial cracks, we assume that the ratio $\bar{\rho}_s$ in Eq. (51) for circular cracks can be extended to

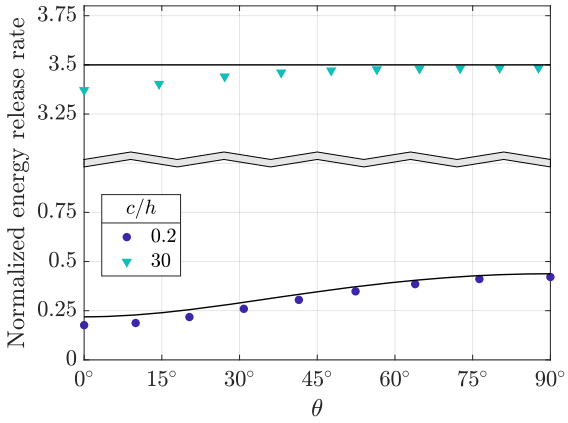

Fig. 19 The normalized energy release rate along the front of a small ($c/h = 0.2$) and a large ($c/h = 30$) interfacial elliptical cracks ($\alpha = 0.5$), versus the angle θ. The analytical solutions, $\bar{g}_s^i$ in Eq. (66) and $\bar{g}_l^i$ in Eq. (65), are shown as lines, and the finite element solutions are shown as symbols. The CM layer is characterized by $\nu = 0.3$ and $\xi = 1/50$

non-circular cracks, and therefore

$$\bar{g}_s^i \approx \bar{\rho}_s(\chi)\, \bar{g}_s^e\left(\chi, \frac{c}{h}, p\right). \tag{66}$$

The accuracy of these approximate solutions is assessed by comparing them to finite element solutions for the two configurations considered in Section 6.4, except that the elliptical cracks are interfacial rather than embedded. Accordingly, results presented in Fig. 19 for the interfacial elliptical cracks resemble those in Fig. 18 for the embedded elliptical cracks. In both figures, the normalized energy release rates for the large cracks are approximately equal. In contrast, the normalized energy release rate for the small elliptical crack in Fig. 19 is approximately half of that in Fig. 18. For both interfacial cracks, the approximate analytical and finite element solutions are in good agreement.

7 Summary

In this paper, we have developed approximate analytical solutions for the energy release rate of embedded and interfacial cracks in constrained elastic thin layers. The accuracy of these solutions has been assessed by comparing them with those obtained by finite element calculations. The main results are summarized as follows.

- For small circular embedded cracks, the energy release rate is linear in the crack radius. Under displacement-controlled boundary conditions, the normalized energy release rate increases significantly with decreasing material compressibility and layer thickness.
- For large circular embedded cracks, the energy release rate approaches a constant (steady state) in compressible thin layers under displacement-controlled boundary conditions. In contrast, the energy release rate decreases with the crack radius in incompressible and nearly incompressible layers.
- Under displacement-controlled boundary conditions, crack growth is unstable for small cracks and transitions to neutral stability with a constant energy release rate (steady state) for large cracks in compressible thin layers. In contrast, for incompressible and nearly incompressible layers, crack growth transitions from unstable to stable.
- Under force-controlled boundary conditions, the energy release rate increases with the crack size for both small and large cracks in compressible layers, and thus crack growth is unstable. In contrast, for incompressible and nearly incompressible layers, crack growth transitions from unstable to stable and then to unstable again. The stable crack growth under the force-controlled condition is rather unusual, which may be attributed to the combined effect of low material compressibility ($\chi \ll 1$) and layer thinness ($\xi \ll 1$).
- For circular interfacial cracks, qualitatively similar analytical solutions are obtained for small and large cracks. It is found that the energy release rate for a small interfacial crack is approximately half of that for an embedded crack of the same size. In contrast, the energy release rate for a large interfacial crack is approximately equal to that for a large embedded crack.
- For compressible thin layers, the approximate analytical solutions can be extended to non-axisymmetric planar cracks for both embedded and interfacial cracks. The solution is particularly simple for large cracks, as it implies approximately constant energy release rate along the crack front, independent of its shape or location. However, this approach cannot be easily extended to cracks in incompressible or nearly incompressible layers.

We believe that this paper has the following contributions to the literature:

- It provides a comprehensive set of approximate analytical solutions for the energy release rate of axisymmetric embedded cracks of small and large sizes in compressible, nearly incompressible, and incompressible thin layers. An important aspect of these solutions is they clearly distinguish between nearly incompressible materials, defined by the condition $\chi \ll 1$, and nearly incompressible layers, defined by the condition $\xi/\chi = \mathcal{O}(1)$.
- It significantly expands and improves on the previous results of Benvidi and Bacca (2021) for axisymmetric interfacial cracks, as it provides accurate asymptotic solutions for both small and large cracks, and the asymptotic solutions for nearly incompressible layers are constructed by properly taking into account the competition between small normalized thickness ξ and small compressibility χ.
- It provides a simple approximate solution for any large planar crack, embedded or interfacial, in compressible thin layers. The simplicity of this solution should be particularly appealing for characterization of thin adhesive layers.

Acknowledgements The authors gratefully acknowledge helpful discussions with Drs. Kenneth M. Liechti and K. Ravi-Chandar of UT Austin.

Appendix A Asymptotic solutions for constrained elastic thin layers

In this appendix, we follow the approach of Movchan et al. (2021) and develop analytical expressions for solid and annular thin layers used in Sect. 2.

Appendix A.1 General solution

A solution of partial differential equations governing axisymmetric problems of classical elasticity can be represented using Love-Galerkin's potential Φ. This potential must satisfy the bi-harmonic equation

$$\left(\frac{\partial^2}{\partial r^2} + \frac{1}{r}\frac{\partial}{\partial r} + \frac{\partial^2}{\partial z^2}\right)^2 \Phi = 0\,, \tag{A.1}$$

where r and z are cylindrical coordinates, such that z is measured along the axis of symmetry. For a given Φ, the displacement components are expressed as

$$u_r = -\frac{1}{2(1-\nu)}\frac{\partial^2 \Phi}{\partial r \partial z}\,, \tag{A.2}$$

and

$$u_z = \frac{\partial^2 \Phi}{\partial r^2} + \frac{1}{r}\frac{\partial \Phi}{\partial r} + \frac{1-2\nu}{2(1-\nu)}\frac{\partial^2 \Phi}{\partial z^2}\,. \tag{A.3}$$

For thin layers, it is advantageous to introduce scaled coordinates

$$R := \frac{r}{a} = \frac{\xi r}{h} \quad \text{and} \quad Z := \frac{z}{h}\,,$$

as they naturally introduce the small parameter $\xi = h/a$ into the problem. As a result, Eqs. (A.1) through (A.3) can be rewritten as

$$\frac{\partial^4 \Phi}{\partial Z^4} = 0\,, \tag{A.4}$$

$$u_r = -\frac{1}{2(1-\nu)}\frac{\xi}{h^2}\frac{\partial^2 \Phi}{\partial R \partial Z}\,, \tag{A.5}$$

and

$$u_z = \frac{\xi^2}{h^2}\left[\frac{\partial^2 \Phi}{\partial R^2} + \frac{1}{R}\frac{\partial \Phi}{\partial R}\right] + \frac{1-2\nu}{2(1-\nu)}\frac{1}{h^2}\frac{\partial^2 \Phi}{\partial Z^2}\,. \tag{A.6}$$

Note that Eq. (A.4) implies that Φ is a cubic polynomial in Z.

For constrained thin layers, Φ is taken in the form

$$\Phi = \frac{h^2 \Delta}{2\chi^2} A(R)\left(Z^2 - 3\right) Z\,, \tag{A.7}$$

where $A(R)$ satisfies Bessel's equation

$$-\frac{\xi^2}{\chi^2}\left[A''(R) + \frac{1}{R}A'(R)\right] + A(R) = 1\,. \tag{A.8}$$

With these provisions, the displacements derived from (A.5) and (A.6) satisfy the boundary conditions imposed by the plates.

The general solution of Eq. (A.8) is

$$A(R) = 1 + C_1 I_0\left(\frac{R\chi}{\xi}\right) + C_2 K_0\left(\frac{R\chi}{\xi}\right)\,, \tag{A.9}$$

where C_1 and C_2 are integration constants to be determined by satisfying traction-free boundary-conditions on the cylindrical boundary (boundaries).

Appendix A.2 Solid layer

For a solid thin layer of radius a, the traction-free boundary conditions are satisfied approximately, by requiring

$$\frac{1}{2h}\int_{-h}^{h} \sigma_{rr}\mathrm{d}z = 0 \text{ and } \frac{1}{2h}\int_{-h}^{h} \sigma_{rz}\mathrm{d}z = 0 \text{ at } \quad r = a\,.$$

Of these two conditions, the second one is automatically satisfied due to symmetry, so that the traction-free boundary conditions yield only one non-trivial equation for C_1 and C_2. The second equation is obtained by requiring $A(R)$ to be finite at $R = 0$. As a result, we obtain

$$C_1 = \frac{3\left(3-2\chi^2\right)}{\left(3-\chi^2\right)\left[2\xi\chi I_1\left(\frac{\chi}{\xi}\right) - 3I_0\left(\frac{\chi}{\xi}\right)\right]} \tag{A.10}$$

and

$$C_2 = 0\,. \tag{A.11}$$

Now one can reconstruct $A(R)$ and Φ, calculate the displacements, and then stresses. Of particular interest is the stress σ_{zz} at two locations,

$$\begin{aligned}\sigma_0 &= \sigma_{zz}(R=0, Z=0)\\ &= \left\{1 + \frac{\left(3-2\chi^2\right)\left(6-9\chi^2+2\chi^4\right)}{2\left(3-\chi^2\right)\left[2\xi\chi I_1\left(\frac{\chi}{\xi}\right) - 3I_0\left(\frac{\chi}{\xi}\right)\right]}\right\}\frac{3\mu\Delta}{h\chi^2}\,,\end{aligned} \tag{A.12}$$

and

$$\begin{aligned}\sigma_1 &= \sigma_{zz}(R=0, Z=-1)\\ &= \left\{1 + \frac{9-6\chi^2}{\left(3-\chi^2\right)\left[2\xi\chi I_1\left(\frac{\chi}{\xi}\right) - 3I_0\left(\frac{\chi}{\xi}\right)\right]}\right\}\frac{3\mu\Delta}{h\chi^2}\,.\end{aligned} \tag{A.13}$$

The transmitted force is calculated as

$$\begin{aligned}F_s &= 2\pi\int_0^a \sigma_{zz|z=h} r\mathrm{d}r = 2\pi a^2\int_0^1 \sigma_{zz|Z=1} R\mathrm{d}R =\\ &\frac{3\pi\mu a^2\Delta}{\chi^3\left(3-\chi^2\right)h}\\ &\left[\frac{3\chi\left(3-\chi^2\right)I_0\left(\frac{\chi}{\xi}\right) - 2\xi\left(-\chi^4-3\chi^2+9\right)I_1\left(\frac{\chi}{\xi}\right)}{3I_0\left(\frac{\chi}{\xi}\right) - 2\xi\chi I_1\left(\frac{\chi}{\xi}\right)}\right].\end{aligned} \tag{A.14}$$

For incompressible materials,

$$\tilde{F}_s := \lim_{\chi\to 0} F_s = \frac{3\pi\mu a^2}{8\xi^2}\frac{\Delta}{h}\,. \tag{A.15}$$

Appendix A.3 Annular layer

For an annular layer with the inner radius $c = \varsigma a$ and the outer radius a, the traction-free boundary conditions are imposed at $r = c$ and $r = a$. As a result, we obtain

$$\begin{aligned}C_1 = \frac{3\left(3-2\chi^2\right)}{D} \times \Big\{&3\varsigma\left[K_0\left(\frac{\chi}{\xi}\right) - \varsigma K_0\left(\frac{\chi\varsigma}{\xi}\right)\right]\\ &+2\xi\chi\left[\varsigma K_1\left(\frac{\chi}{\xi}\right) - K_1\left(\frac{\chi\varsigma}{\xi}\right)\right]\Big\}\,,\end{aligned} \tag{A.16}$$

$$\begin{aligned}C_2 = \frac{3\left(3-2\chi^2\right)}{D} \times \Big\{&-3\varsigma\left[I_0\left(\frac{\chi}{\xi}\right) - \varsigma I_0\left(\frac{\chi\varsigma}{\xi}\right)\right]\\ &+2\xi\chi\left[\varsigma I_1\left(\frac{\chi}{\xi}\right) - I_1\left(\frac{\chi\varsigma}{\xi}\right)\right]\Big\}\,,\end{aligned} \tag{A.17}$$

with

$$\begin{aligned}D = \left(3-\chi^2\right)\Big\{&4\xi^2\chi^2\left[K_1\left(\frac{\chi}{\xi}\right)I_1\left(\frac{\chi\varsigma}{\xi}\right)\right.\\ &\left.-I_1\left(\frac{\chi}{\xi}\right)K_1\left(\frac{\chi\varsigma}{\xi}\right)\right]\\ &+6\xi\chi\left[K_0\left(\frac{\chi}{\xi}\right)I_1\left(\frac{\chi\varsigma}{\xi}\right) + I_0\left(\frac{\chi}{\xi}\right)K_1\left(\frac{\chi\varsigma}{\xi}\right)\right]\\ &-6\xi\chi\varsigma\left[K_1\left(\frac{\chi}{\xi}\right)I_0\left(\frac{\chi\varsigma}{\xi}\right) + I_1\left(\frac{\chi}{\xi}\right)K_0\left(\frac{\chi\varsigma}{\xi}\right)\right]\\ &-9\varsigma\left[K_0\left(\frac{\chi}{\xi}\right)I_0\left(\frac{\chi\varsigma}{\xi}\right) - I_0\left(\frac{\chi}{\xi}\right)K_0\left(\frac{\chi\varsigma}{\xi}\right)\right]\Big\}\,.\end{aligned} \tag{A.18}$$

The transmitted force is calculated as

$$\begin{aligned}F_l = 2\pi\int_c^a \sigma_{zz|z=h} r\mathrm{d}r = 2\pi a^2\int_0^\varsigma \sigma_{zz|Z=1} R\mathrm{d}R =\\ \frac{3\pi\mu a^2(1-\varsigma^2)\Delta}{\chi^2 h} + \frac{6\pi\mu a^2\xi\Delta}{\chi^3 h}\\ \times\left\{\left[I_1\left(\frac{\chi}{\xi}\right) - \varsigma I_1\left(\frac{\chi\varsigma}{\xi}\right)\right]C_1\right.\\ \left.-\left[K_1\left(\frac{\chi}{\xi}\right) - \varsigma K_1\left(\frac{\chi\varsigma}{\xi}\right)\right]C_2\right\}\,.\end{aligned} \tag{A.19}$$

An explicit form of this equation is too cumbersome to be useful.

References

Abramowitz M, Stegun IA (1968) Handbook of mathematical functions with formulas, graphs, and mathematical tables. volume volume55. publisherUS Government printing office

Anderson ML, Mott PH, Roland CM (2004) The compression of bonded rubber disks. Rubber Chem Technol 77:293–302

Bayraktar E, Bessri K, Bathias C (2008) Deformation behaviour of elastomeric matrix composites under static loading conditions. Eng Fracture Mech 75:2695–2706

Benvidi FH, Bacca M (2021) Theoretical limits in detachment strength for axisymmetric bi-material adhesives. J Appl Mech 88:121007

Biggins JS, Saintyves B, Wei Z, Bouchaud E, Mahadevan L (2013) Digital instability of a confined elastic meniscus. Proc Natl Acad Sci 110:12545–12548

Creton C, Ciccotti M (2016) Fracture and adhesion of soft materials: a review. Rep Prog Phys 79:046601

Crosby AJ, Shull KR, Lakrout H, Creton C (2000) Deformation and failure modes of adhesively bonded elastic layers. J Appl Phys 88:2956–2966

Filon LNG (1902) Iv. on the elastic equilibrium of circular cylinders under certain practical systems of load. Philosophical Transactions of the Royal Society of London. Series A, Contain Papers Math Phys Charact 198:147–233

Fischer SC, Arzt E, Hensel R (2017) Composite pillars with a tunable interface for adhesion to rough substrates. ACS Appl Mater Interfaces 9:1036–1044

Fond C (2001) Cavitation criterion for rubber materials: a review of void-growth models. J Polym Sci Part B 39:2081–2096

Gent AN, Lindley PB (1959) Internal rupture of bonded rubber cylinders in tension Proceedings of the Royal Society of London. Series A. Math Phys Sci 249:195–205

Green A, Sneddon I (1950) The distribution of stress in the neighbourhood of a flat elliptical crack in an elastic solid, in: booktitleMathematical Proceedings of the Cambridge Philosophical Society, organizationCambridge University Press. pp. 159–163

Guo J, Ravi-Chandar K (2023) On crack nucleation and propagation in elastomers: I. In situ optical and X-ray experimental observations. Int J Fracture 243:1–29

Hao S, Suo Z, Huang R (2023) Why does an elastomer layer confined between two rigid blocks grow numerous cavities? J Mech Phys Solids 173:105223

Hensel R, McMeeking RM, Kossa A (2019) Adhesion of a rigid punch to a confined elastic layer revisited. J Adhesion 95:44–63

Horváth AL, Kossa A (2024) Stability maps for the slightly compressible poker chip detachment problem. Finite Elements Anal Design 242:104257

Hutchinson JW, Suo Z (1991) Mixed mode cracking in layered materials. Adv Appl Mech 29:63–191

Irwin GR (1962) Crack-extension force for a part-through crack in a plate. J Appl Mech 29:651–654

Kanninen MF, Popelar CH (1985) Advanced fracture mechanics. Oxford engineering science series, 15, publisherOxford University Press, addressNew York

Kassir MK, Bregman AM (1972) The stress-intensity factor for a penny-shaped crack between two dissimilar materials. J Appl Mech 39:308–310

Kelly JM, Konstantinidis D (2011) Mechanics of rubber bearings for seismic and vibration isolation. John Wiley, Hoboken

Kumar A, Lopez-Pamies O (2021) The poker-chip experiments of Gent and Lindley (1959) explained. J Mech Phys Solids 150:104359

Lin S, Mao Y, Radovitzky R, Zhao X (2017) Instabilities in confined elastic layers under tension: fringe, fingering and cavitation. J Mech Phys Solids 106:229–256

Lin Y, Hui C, Conway H (2000) A detailed elastic analysis of the flat punch (tack) test for pressure-sensitive adhesives. J Polym Sci Part B - Polym Phys 38:2769–2784

Lindsey GH (1967) Triaxial fracture studies. J Appl Phys 38:4843–4852

Lindsey GH, Schapery RA, Williams ML, Zak AR (1963) The triaxial tension failure of viscoelastic materials. typeTechnical Report number63-152. Aerospace Research Laboratories

Malyshev B, Salganik R (1965) The strength of adhesive joints using the theory of cracks. Int J Fracture 1:1–29

Mear ME, Rodin GJ (2011) An isolated mode I three-dimensional planar crack: the stress intensity factor is independent of the elastic constants. Int J Fracture 172:217–218

Minsky H, Turner K (2015) Achieving enhanced and tunable adhesion via composite posts. Appl Phys Lett 106:201604

Movchan A, Movchan N, Rodin G (2023) Asymptotic analysis of thin linear elastic layers constrained by two rigid plates. Int J Solids Struct 285:112561

Movchan AB, Rebrov KR, Rodin GJ (2021) Axisymmetric deformation of compressible, nearly incompressible, and incompressible thin layers between two rigid surfaces. Int J Solids Struct 214:61–73

Reynolds O (1886) On the Theory of Lubrication and Its Application to Mr. Beauchamp Tower's Experiments, Including an Experimental Determination of the Viscosity of Olive Oil. Philos Trans Royal Soc London. Series A 177:157–234

Rice JR (1988) Elastic fracture mechanics concepts for interfacial cracks. J Appl Mech 55:98–103

Sadowsky M, Sternberg E (1949) Stress concentration around a triaxial ellipsoidal cavity. J Appl Mech 16:149–157

Shull KR, Creton C (2004) Deformation behavior of thin, compliant layers under tensile loading conditions. J Polym Sci Part B: Polym Phys 42:4023–4043

Stefan J (1874) Versuche über die scheinbare Adhäsion. Sitzungsberichte der Kaiserlichen Akademie der Wissenschaften. Mathematisch-Naturwissenschaftliche Classe 69, 713–735

Tada H, Paris PC, Irwin GR, (1973) The stress analysis of cracks handbook. publisherDel Research Corporation

Warn GP, Ryan KL (2012) A review of seismic isolation for buildings: historical development and research needs. Buildings 2:300–325

Webber RE, Shull KR, Roos A, Creton C (2003) Effects of geometric confinement on the adhesive debonding of soft elastic solids. Phys Rev E 68:021805